Since January 2020 Elsevier has created a COVID-19 resource centre with free information in English and Mandarin on the novel coronavirus COVID-19. The COVID-19 resource centre is hosted on Elsevier Connect, the company's public news and information website.

Journal of Molecular Structure 1232 (2021) 130005

Contents lists available at ScienceDirect

Journal of Molecular Structure

journal homepage: www.elsevier.com/locate/molstr

5-((1H-imidazol-1-yl)methyl)quinolin-8-ol as potential antiviral SARS-CoV-2 candidate: Synthesis, crystal structure, Hirshfeld surface analysis, DFT and molecular docking studies ☆

Dhaybia Douche [a], Yusuf Sert [b], Silvia A. Brandán [c,*], Ameed Ahmed Kawther [d], Bayram Bilmez [d], Necmi Dege [d], Ahmed El Louzi [a], Khalid Bougrin [a,e], Khalid Karrouchi [f,*], Banacer Himmi [a,g]

[a] Equipe de Chimie des Plantes et de Synthèse Organique et Bioorganique-URAC23, GEOPAC, Département de Chimie, Faculté des Sciences, Université Mohammed V in Rabat, Morocco
[b] Sorgun Vocational School, Science and Art Faculty-Department of Physics, Yozgat Bozok University, Yozgat, Turkey
[c] Cátedra de Química General, Instituto de Química Inorgánica, Facultad de Bioquímica, Química y Farmacia, Universidad Nacional de Tucumán, Ayacucho 471, 4000, Tucumán, Argentina
[d] Department of Physics, Faculty of Arts and Sciences, Ondokuz Mayıs University, Samsun, Turkey
[e] Chemical & Biochemical Sciences Green-Process Engineering (CBS-GPE) Mohammed VI Polytechnic University, Lot 660, Hay Moulay Rachid, Benguerir, Morocco
[f] Laboratory of Analytical Chemistry and Bromatology, Faculty of Medicine and Pharmacy, Mohammed V University in Rabat, Morocco
[g] Filière Techniques de Santé, Institut Supérieur des Professions Infirmières et Techniques de Santé de Rabat, Ministère de la Santé, Morocco

ARTICLE INFO

Article history:
Received 25 November 2020
Revised 8 January 2021
Accepted 15 January 2021
Available online 27 January 2021

Keywords:
Quinoline
X-ray
DFT
Hirshfeld surface analysis
Molecular docking
Coronavirus

ABSTRACT

A potential new drug to treat SARS-CoV-2 infections and chloroquine analogue, 5-((1H-imidazol-1-yl)methyl)quinolin-8-ol (**DD1**) has been here synthesized and characterized by FT-IR, ^{1}H-NMR, ^{13}C-NMR, ultraviolet-visible, ESI-MS and single-crystal X-ray diffraction. **DD1** was optimized in gas phase, aqueous and DMSO solutions using hybrid B3LYP/6-311++G(d,p) method. Comparisons between experimental and theoretical infrared spectra, ^{1}H and ^{13}C NMR chemical shifts and electronic spectrum in DMSO solution evidence good concordances. Higher solvation energy was observed in aqueous solution than in DMSO, showing in aqueous solution a higher value than antiviral brincidofovir and chloroquine. on Bond orders, atomic charges and topological studies suggest that imidazole ring play a very important role in the properties of **DD1**. NBO and AIM analyses support the intra-molecular O15-H16•••N17 bonds of **DD1** in the three media. Low gap value supports the higher reactivity of DD1 than chloroquine justified by the higher electrophilicity and low nucleophilicity. Complete vibrational assignments of **DD1** in gas phase and aqueous solution are reported together with the scaled force constants. In addition, better intermolecular interactions were observed by Hirshfeld surface analysis. Finally, the molecular docking mechanism between **DD1** ligand and COVID-19/6WCF and COVID-19/6Y84 receptors were studied to explore the binding modes of these compounds at the active sites. Molecular docking results have shown that the **DD1** molecule can be considered as a potential agent against COVID-19/6Y84-6WCF receptors.

1. Introduction

Quinoline and its derivatives have always attracted both synthetic and biological chemist because of its diverse chemical and pharmacological properties [1-6]. Literature survey revealed that quinoline derivatives had shown potency as antiviral agents against several viruses such as human immunodeficiency virus, Zika virus, H1N1 influenza virus, Hepatitis C virus, dengue virus, vaccinia virus and respiratory syncytial virus [7-13]. On the other hand, several authors report the antiviral potential of chloroquine as a

☆ **Supplementary crystallographic data:** CCDC 2005089 for **DD1**, contain the supplementary crystallographic data for these compounds, and can be obtained free of charge from the Cambridge Crystallographic Data Centre via www.ccdc.cam.ac.uk/data_request/cif.

* Corresponding authors.
E-mail addresses: silvia.brandan@fbqf.unt.edu.ar (S.A. Brandán), Khalid.karrouchi@um5s.net.ma (K. Karrouchi).

https://doi.org/10.1016/j.molstruc.2021.130005
0022-2860/

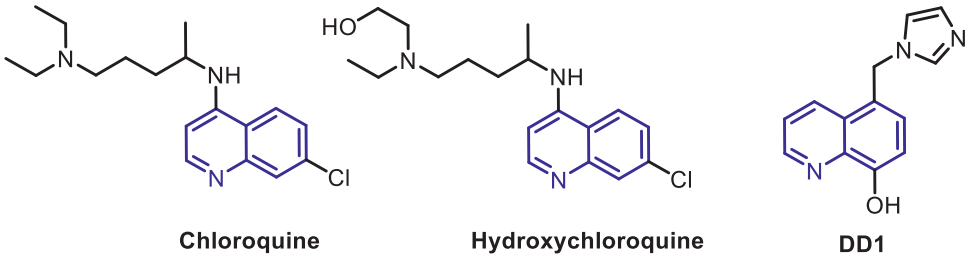

Fig. 1. Molecular structures of Chloroquine, Hydroxychloroquine, and **DD1**.

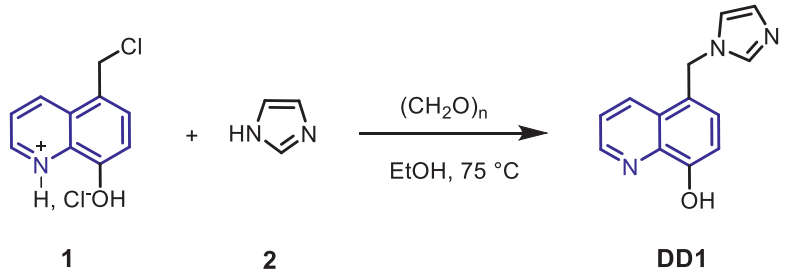

Scheme 1. Synthetic route of **DD1**.

therapeutic option against COVID-19, this quinoline derivative presented an EC_{50} of 1.13 μM *in vitro* and it caused a negative conversion of the virus in more than 100 patients who participated in multicenter clinical trials conducted in China (*in vivo*) [14,15]. In the *in vitro* study recently carried out by Liu et *al.* [16] have shown that chloroquine and hydroxychloroquine prevent the virus from entering the cell and block the transport of the virus between cell organelles at the later cellular stages of SARS-CoV-2 infection. However, chloroquine has been shown to have higher efficacy [16]. On the other hand, hydroxychloroquine (Fig. 1) has been demonstrated to have an anti-SARS-CoV activity *in vitro* [17]. A clinical trial using hydroxychloroquine has been conducted in patients infected with SARS-CoV-2. The first results show a significant reduction in viral carriage and the use of hydroxychloroquine added to Azithromycin was significantly more efficient for virus elimination [18].

In view of the therapeutic properties of quinoleine derivatives, the investigation of their molecular geometric structure, spectroscopic and electronic properties are fundamental to know the influence of different groups on structures in order to discover the relationship of these groups with their biological properties. In this context, DFT calculations have become a tool very reliable in predicting properties of molecules with great precision [19-25].

Since the quinoline derivatives have shown high potential for the development of new antiviral drugs, herein, we have designed novel 8-hydroxyquinoline derivative i.e, 5-((*1H*-imidazol-1-yl)methyl)quinolin-8-ol (**DD1**) (Fig. 1).

Scheme 1

This new 8-hydroxyquinoline derivative was synthesized and characterized by using FT-IR, UV-visible, ^{1}H- and ^{13}C-NMR, ESI-MS and single-crystal X-ray diffraction. Then, theoretical B3LYP/6-311++G** calculations were performed to explore its structural, electronic, topological and vibrational properties in gas phase and aqueous and DMSO solutions [26,27]. Thus, with the optimized structures in the different media additional calculations by using the same level of theory were carried out to calculate atomic charges, stabilization energies, bond orders, molecular electrostatic potentials, vibrational frequencies, ^{1}H and ^{13}C NMR chemical shifts and Hirshfeld surface analysis. Due to the importance of this derivative, calculations of frontier orbitals also were performed in order to predict the reactivities and behaviours of **DD1** in the different studied media. Finally, the molecular docking mechanism between **DD1** ligand and COVID-19/6WCF and COVID-19/6Y84 receptors were studied to explore the binding modes of these compounds at the active sites.

2. Experimental section

2.1. General methods

All organic solvents were purchased from commercial sources and used as received or dried using standard procedures; all chemicals were purchased from Aldrich, Merck or Alfa Aesar and used without further purification. Analytical thin layer-chromatographies (TLC) have been performed on pre-coated silica gel plates (Kieselgel 60 F_{254}, Merck, Germany), and chromatograms were visualized by UV- light irradiation. NMR spectroscopies were recorded in dry deuterated DMSO on a Bruker AC spectrometer at 300 MHz for ^{1}H NMR and 75 MHz for ^{13}C NMR; δ is expressed in ppm related to TMS (0 ppm) as internal standard. Splitting patterns are designated as follow: s (singlet), d (doublet), t (triplet), m (multiplet). Coupling constants (*J* values) are listed in Hertz (Hz). Mass spectra were obtained using an API 3200 LC/MS/MS system equipped with an ESI source and the samples were diluted in methanol.

2.2. Synthesis

An equimolar mixture of the 5-(chloromethyl) quinolin-8-ol hydrochloride (0.57 g, 2.5 mmol), paraformaldehyde (0.075 g, 2.5 mmol), and 1H-imidazole (0.17 g, 2.5 mmol) in EtOH (30 mL) was refluxed for 4-5 h. After cooling, the solvent was evaporated under vacuum and the residue was purified through silica gel column chromatography using hexane/ethyl acetate (ratio 5:5). Green single crystals were obtained by slow evaporation at room temperature.

5-((1H-imidazol-1-yl)methyl)quinolin-8-ol (**DD1**). Yield = 35%; mp = 184-186°C; ^{1}H-NMR (300 MHz, DMSO-d_6, δ(ppm)): 5.56 (s, 2H, CH_2), 6.84 (d, J=2Hz, 1H, H4-imidazole), 7.05 (d, J=4Hz, 1H, H7- quinoline), 7.10 (d, J=2Hz, 1H, H4-imidazole), 7.36 (d, J=5Hz, 1H, H-6 quinoline), 7.58 (t, J=8.0Hz, J=4Hz, H-3 quinoline), 7.75 (s, 1H, H2-imidazole), 8.53 (dd, J=8Hz, J=2Hz, H-4 quinoline) 8.85

(dd, J=8Hz, J=2Hz, 1H, H-2 quinoline), 9.93 (s, 1H, OH). ^{13}C NMR spectrum (75 MHz, DMSO-d_6) δ, ppm: 46.88, 111.01, 119.89, 122.59, 123.55, 127.06, 128.91, 132.55, 137.77, 139.13, 148.45, 154.01. ESI-MS: m/z = 226.1 $[M+H]^+$, 248.4 $[M+Na]^+$.

2.3. X-ray analysis

The X-ray intensity data for **DD1** were collected at 296 K on a STOE *IPDS* 2 diffractometer equipped with an X-ray generator operating at 50 kV and 1 mA, using Mo-Kα radiation of wavelength 1.54178 Å. The hemisphere of data was processed using *SAINT* [28]. The 3D structure was solved by direct methods and refined by full-matrix least squares method on F^2 using the *SHELXL* program [29,30]. All the non-hydrogen atoms were revealed in the first difference Fourier map and were refined with isotropic displacement parameters. At the end of the refinement, the final difference Fourier map showed no peaks of chemical significance and the final residual was 0.0641. The molecular and packing diagrams were generated using DIAMOND [31].

2.4. Computational details

The theoretical initial structure of **DD1** was taken from the CIF file determined in this work by X-ray diffraction. Then, the optimizations were performed in gas phase and aqueous and DMSO solutions by using the functional hybrid B3LYP and the 6-311++G** basis set with the Revision A.02 of Gaussian 09 program [26,27,32]. In this type of molecule the used method performs the better correlations in geometries and frequencies, as was observed by us for other species [19-22]. The integral equation formalism variant polarised continuum model (IEFPCM) method and the solvation model were used for the optimizations in solution by using the same level of theory [33-35]. Atomic charges and topological properties were computed with natural bond orbital (NBO) and atoms in molecules (AIM) calculations [36-38] while the *GaussView* program was employed to graphic the mapped molecular electrostatic potentials (MEP) obtained from the Merz-Kollman (MK) charges [39,40]. In the vibrational study, normal internal coordinates and transferable scaling factors were used to calculate the harmonic force fields in the different media with the scaled quantum mechanical force field (SQMFF) methodology and the Molvib program [41-43]. In the assignments only those potential energy distribution (PED) contributions $\geq$ 10% were considered while the correlations in the Raman spectra were improved transforming the predicted spectra in activities to intensities, as suggested in the literature [44,45]. The ^{1}H- and ^{13}C-NMR spectra in aqueous and DMSO solutions were predicted with the Gauge-Independent Atomic Orbital (GIAO) method [46] with the hybrid B3LYP/6-311++G** method while the electronic spectra at the same level of theory were also predicted by using Time-dependent DFT calculations (TD-DFT) and the Gaussian 09 program [32]. The Moldraw program was used to calculate the volumes variations that experiment **DD1** in aqueous and DMSO solutions [47]. The gap values and the chemical potential (μ), electronegativity (χ), global hardness (η), global softness (S), global electrophilicity index (ω) and nucleophilicity indexes (E) descriptors were calculated from the frontier orbitals with the same level of theory and by using known equations [19-22]. In this new derivative is useful to predict the reactivities and behaviours in the different media taking into account the presence of donor (OH) and acceptors (O and N) groups in the structure of **DD1** [48,49]. The molecular docking mechanism between **DD1** ligand and COVID-19/6WCF and COVID-19/6Y84 receptors were studied by using AutoDock Vina free software program [50].

3. Results and discussion

3.1. X-ray crystal structure description

The details of the X-ray crystal data and the structure solution as well as the refinement of the title compounds are given in Table 1. Supplementary data are deposited at CCDC under deposition numbers 2005089 for **DD1**. The title compounds crystalized in the monoclinic system. The experimental molecular structure of compound **DD1** is illustrated in Fig. 2.

In the title molecule, the phenyl ring (C4–C9) and pyridine ring (N1/C1/C2/C3/C4/C9) are almost planar, making a dihedral angle of 1.805 (1)°; the imidazole ring (N2/C11/C12/N3/C13) is twisted with respect to phenyl ring (C4–C9) with a dihedral angle of 65.233 (1)°; and the dihedral angle between imidazole and pyridine rings is 66.968 (1)°.

For **DD1**, the torsion angles are, 70.60 (1)° in C11–N2–C10–C5, -110.07 (1)° in C13–N2–C10–C5, 89.30 (1)° in C6–C5–C10–N2, -93.01 (1)° in C4–C5–C10–N2. In the title compound, molecules are linked by O–H•••N hydrogen bonds (Fig. 3 and Table 2).

3.2. Molecular Geometric Structures in different media

The hybrid B3LYP/6-311++G** method has optimized the structures of 5-((1H-imidazol-1-yl)methyl)quinolin-8-ol (**DD1**) in all media with C_1 symmetries where the structure in gas phase compared with the corresponding experimental determined by X-ray diffraction together with the definitions of rings can be seen in Fig. 4. R1 corresponds to pyridine ring, R2 to phenyl ring containing the OH group while the imidazol ring is defined as R3. In **Table 3** are presented total energies uncorrected and corrected by zero point vibrational energy (ZPVE), dipole moments and volumes of **DD1** in gas phase and aqueous and DMSO solutions by using the B3LYP/6-311++g(d,p) Method. The three calculations evidence a higher stability of structure in gas phase while in aqueous and DMSO solutions the energy values increase notably being slightly less stable in water than DMSO solvent. Perhaps, the higher dipole moment and volume values of **DD1** in water justify its lower stability in this medium. In both solvents there is a contraction in the volume when dissolving is performed but, the value is higher in DMSO solution probably due to its higher stability and low dissolution (-1.6 Å^3). Thus, the solvent effect can be observed in graphics of orientations and directions of dipole moment vectors because the magnitude is higher in water (**Figure S1**).

Due to the difference observed in the properties of DD1 in both solvents it is necessary to calculate the solvation energies in the two solvents. Hence, the corrected and uncorrected solvation energies in both solvents calculated from the energies ZPVE can be seen in **Table 4**.

The results shown in Table 4 have evidenced most negative solvation energy of **DD1** in water, as expected because this new derivative is most stable in DMSO. Hence, the ΔG_c value for the water was obtained from the difference between $\Delta G_{un}{}^{\#}$ and ΔG_{ne}, that is, -471.09 - 15.13 = -486.22 kJ/mol. In the same way, in DMSO, the values are: -457.71 – (-7.73) = -449.98 kJ/mol. Note that the total non-electrostatic terms (ΔG_{ne}) present different signs in both solvents, thus, in water that term is positive while in DMSO it has a negative value. The high solvation energy values of **DD1** in both media suggest that the acceptors groups (N and O) probably are protonated and charged because previous studies on some antiviral, antihistaminic and alkaloids species have evidenced that in aqueous solution the forms hydrated or cationic present a higher value as compared with the neutral free base or hydrochloride species [51-59], as can be observed in **Table S1**. If now the (ΔG_c) values of DD1 in aqueous solution are compared with reported

Table 1
Crystal data, data collection and structure refinement details for **DD1**.

Crystal data	
Chemical formula	$C_{13}H_{11}N_3O$
M_r	225.25
Crystal system, space group	Monoclinic, $P2_1/n$
Temperature (K)	296
a, *b*, *c* (Å)	10.2882 (5), 9.7521 (6), 11.0496 (5)
β (°)	104.134 (4)
V (Å^3)	1075.06 (10)
Z	4
Radiation type	Mo $K\alpha$
μ (mm^{-1})	0.09
Crystal size (mm)	0.78 × 0.60 × 0.49
Data collection	
Diffractometer	STOE *IPDS* 2
Absorption correction	Integration (*X-RED32*; Stoe & Cie, 2002)
T_{min}, T_{max}	0.958, 0.979
No. of measured, independent and observed [$I > 2\sigma(I)$] reflections	11136, 3202, 2026
R_{int}	0.033
$(\sin\theta/\lambda)_{max}$ (Å^{-1})	0.710
Refinement	
$R[F^2 > 2\sigma(F^2)]$, $wR(F^2)$, *S*	0.042, 0.111, 1.00
No. of reflections	3202
No. of parameters	155
H-atom treatment	H-atom parameters constrained
$\Delta\rho_{max}$, $\Delta\rho_{min}$ (e Å^{-3})	0.17, −0.14

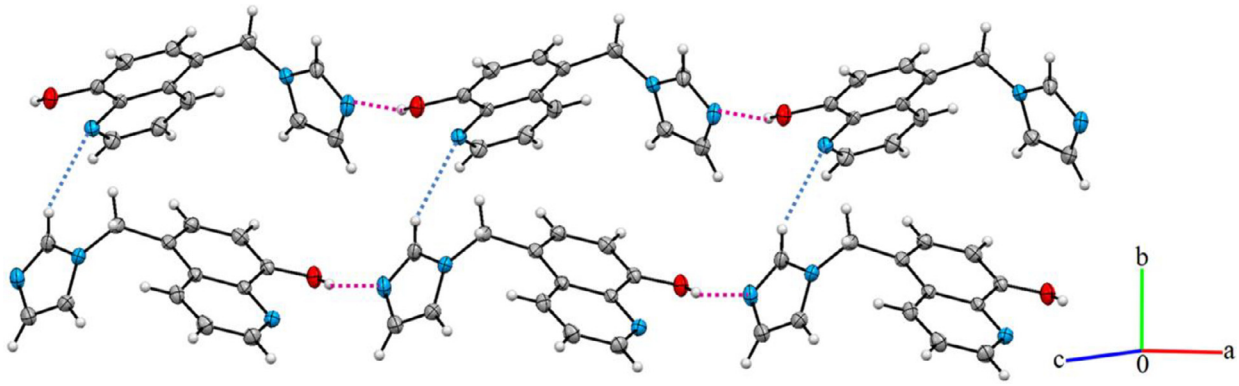

Fig. 2. The molecular structure (ORTEP) of the compounds **DD1**.

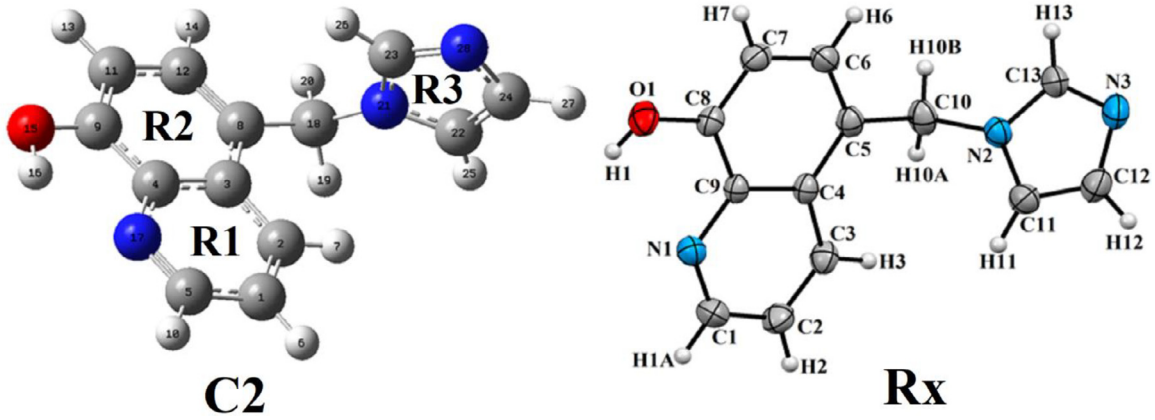

Fig. 3. A view of the crystal packing of compound **DD1** with O—H•••N and C—H•••N hydrogen bonds.

for antiviral species in aqueous solution from **Table S2** [60-65] we observed that **DD1** has the lowest (ΔG_c) value than the antiviral agents, perhaps due to the three rings present in its structure because the number of acceptors and donors is less than the other ones. From previous studies, we observed that the differences in the solvation energies with another smaller basis set do not present greater differences with those calculated with a higher level of theory [22,61,65].

Table 5 show comparisons of calculated geometrical parameters of 5-((1H-imidazol-1-yl)methyl)quinolin-8-ol (**DD1**) in gas phase and aqueous and DMSO solutions with the corresponding experimental determined by X-ray diffraction by using root-mean-square

Table 2
Hydrogen-bond geometry (Å, °) for **DD1**.

D—H•••*A*	*D*—H	*H*•••*A*	*D*•••*A*	*D*—H•••*A*
O1—H1•••N3^{i}	0. 82	1.92	2.701 (15)	157.9

Symmetry code: (i) *x+1, y, z*

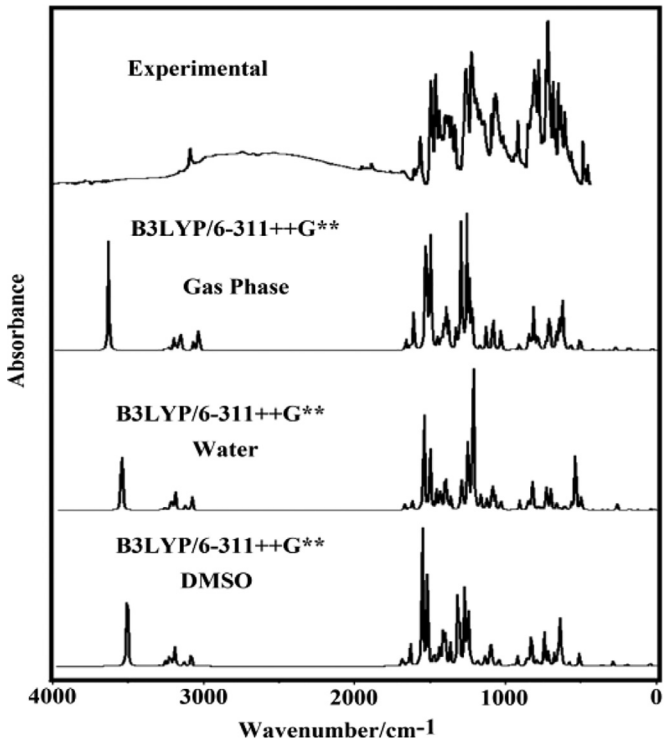

Fig. 4. Comparisons between the most stable theoretical and experimental **DD1** structures, definitions of rings and atoms labeling.

Table 3
Calculated total energies (*E*), dipole moments (μ) and volumes (V) of 5-((1H-imidazol-1-yl)methyl)quinolin-8-ol in gas phase and aqueous and DMSO solutions by using the B3LYP/6-311++g(d,p) Method.

B3LYP/6-311++G(d,p) Method Medium	E (Hartrees)	E_{ZPVE} (Hartrees)	μ (D)	V (Å^3)	ΔV (Å^3)
Gas phase	-741.6819	-741.4622	4.03	238.8	-
Water	-741.5023	-741.2810	5.93	237.6	1.2
DMSO	-741.5074	-741.2859	5.83	237.2	-1.6

deviation (RMSD) values. These calculations were performed at the same level of theory.

The results shown in Table 5 evidence reasonable correlations in bond lengths (0.039-0.037 Å) and angles (1.1-1.0 °) while higher RMSD values are predicted for the dihedral angles with values between 136.9 and 15 °. Some parameters for **DD1** in the three media are overestimated such as, the bond O15-H16 lengths which are longer in the three media than the experimental one probably due to that the calculations show an intra-molecular O-H•••N bond, observing the higher value in DMSO solution, as can be seen in **Figure S2**. On the contrary, the calculations underestimated the C9-O15-H16 angles showing values between 106.0 and 104.9 ° different from the experimental one of 109.5 °. Here, the contractions of volumes in both solvents are evident compared with the value in gas phase. Note that this angle is higher in water, as expected because the hydration is higher in water due to its higher solvation energy value. The dihedral H16-O15-C9-C4 and H16-O15-C9-C11 angles show interesting results in solution because the first one has negative sign in DMSO solution while the second

Table 4
Corrected (ΔG_{cZPVE}) and uncorrected (ΔG_c) solvation energies by the total non-electrostatic terms and by zero point vibrational energy (ZPVE) of 5-((1H-imidazol-1-yl)methyl)quinolin-8-ol in aqueous and DMSO solutions by using the B3LYP/6-311++G(d,p) method.

B3LYP/6-311++G(d,p) Method[a] Solvation energy (kJ/mol)				
Species	$\Delta G_{un}^{\#}$	ΔG_{ne}	ΔG_c	ΔG_{cZPVE}
Water	-471.09	15.13	-486.22	-490.41
DMSO	-457.71	-7.73	-449.98	-454.70

$\Delta G_{un}^{\#}$= uncorrected solvation energy, ΔG_{ne}= total non-electrostatic terms, ΔG_c= corrected solvation energies.
[a] This work

Table 5
Comparisons of calculated geometrical parameters of 5-((1H-imidazol-1-yl)methyl)quinolin-8-ol in gas phase and aqueous and DMSO solutions with the corresponding experimental ones.

B3LYP/6-311++g(d,p) Method Parameters	Gas phase	Water	DMSO	Experimental[a]
Bond lengths (Å)				
C8-C18	1.510	1.510	1.511	1.517
C8-C12	1.380	1.383	1.383	1.369
C12-C11	1.411	1.413	1.413	1.400
C11-C9	1.375	1.377	1.378	1.371
C9-O15	1.346	1.363	1.351	1.341
C9-C4	1.430	1.429	1.431	1.426
O15-H16	0.975	0.981	0.984	0.820
C4-C3	1.424	1.426	1.425	1.423
C3-C8	1.429	1.431	1.432	1.419
C3-C2	1.418	1.420	1.420	1.416
C2-C1	1.375	1.377	1.378	1.352
C1-C5	1.411	1.412	1.413	1.394
C5-N17	1.317	1.322	1.321	1.311
N17-C4	1.356	1.362	1.360	1.364
C18-N21	1.470	1.475	1.475	1.467
N21-C22	1.381	1.380	1.380	1.365
C22-C24	1.371	1.371	1.373	1.341
C24-N28	1.374	1.382	1.379	1.365
N28-C23	1.315	1.324	1.322	1.312
C23-N21	1.367	1.361	1.362	1.340
RMSD	**0.037**	**0.039**	**0.039**	
Bond angles (°)				
C18-C8-C3	121.6	121.7	121.7	121.7
C18-C8-C12	119.9	119.6	119.7	119.7
C8-C12-C11	122.9	122.6	122.9	122.7
C12-C11-C9	119.5	119.5	119.5	120.4
C11-C9-C4	119.6	120.1	119.6	118.9
C9-C4-C3	120.2	119.8	120.3	120.1
C4-C3-C8	119.1	119.2	119.0	119.3
C3-C8-C12	118.3	118.5	118.4	118.6
C4-C3-C2	115.8	116.0	115.8	115.9
C3-C2-C1	119.8	119.7	119.8	120.1
C2-C1-C5	119.3	119.3	119.3	119.4
C1-C5-N17	122.8	123.2	122.8	124.0
C5-N17-C4	118.2	117.7	118.1	117.4
N17-C4-C3	123.7	123.8	123.9	123.1
C9-O15-H16	106.0	105.4	104.9	109.5
C8-C18-N21	114.1	113.6	113.7	113.4
C18-N21-C23	127.7	127.3	127.0	125.9
C18-N21-C22	125.7	125.9	126.0	127.7
N21-C23-N28	112.0	112.3	112.1	112.1
C23-N28-C24	105.3	104.6	105.0	104.8
N28-C24-C22	110.3	110.5	110.3	110.4
C24-C22-N21	105.7	105.7	105.7	106.3
C22-N21-C23	106.3	106.6	106.7	106.4
RMSD	**1.0**	**1.1**	**1.1**	
Dihedral angles (°)				
C18-C8-C3-C2	2.006	0.245	0.125	1.230
C18-C8-C12-H14	-1.666	-0.381	-0.337	-3.491
H16-O15-C9-C4	0.155	0.289	-0.155	-26.221
H16-O15-C9-C11	-179.856	-179.799	179.745	154.383
O15-C9-C11-H13	0.062	-0.174	-0.139	2.0387
C5-N17-C4-C9	179.990	179.800	179.681	177.617
RMSD	**136.9**	**136.9**	**15**	

[a] This work, Bold letter, RMSD values

one shows negative sign in water and in gas phase. On the other hand, the dihedral O15-C9-C11-H13 angles in both solvents present negative values different from the experimental one with positive sign. Hence, the high RMSD values of dihedral angles reveal higher changes in water than DMSO solution, as expected because this new derivative presents higher solvation energy in aqueous solution.

3.3. Atomic charges, molecular electrostatic potentials and bond orders

As was above mentioned, the high solvation energy values of **DD1** in both media could be attributed to that the acceptors (N and O) and donor (OH) groups are protonated and charged and, for these reasons, the calculations related to involved charges on the atoms of those groups are important for this new species as drug candidate [48,49]. Thus, three types of atomics charges, Merz-Kollman (MK), Mulliken and natural population analysis (NPA) charges were calculated on the O15, H16, N17, N21 and N28 atoms of DD1 in gas phase and aqueous and DMSO solutions by using the B3LYP/6-311++G** method [36,39]. These results are summarized in **Table S3** while comparisons among them can be observed in **Figure S3**. Analyzing the MK charges it is observed the same behaviours in the three media with practically the same values and, where the N21 atoms have positive signs while on the N17 and N28 atoms that belong to pyridine and imidazole rings, respectively are observed negative signs. These high negative MK charges observed on N17 and N28 could indicate the formation of H bonds in these sites. However, the Mulliken charges show similar behaviours than the MK ones but the Mulliken charges on the N21 atoms have less positive values and slightly different in the three media. Note that on the N17 and N28 atoms are predicted different Mulliken charges, a resulted different from the MK charges. On the other hand, on the three N atoms are predicted negative NPA charges presenting on the N21 atom in water a less negative value while the most negative values are observed on this same atom in the other two media.

In **Table S4** are shown the molecular electrostatic potentials (MEP) and bond orders (BO), expressed as Wiberg indexes for **DD1** in gas phase and aqueous and DMSO solutions by using B3LYP/6-311++G** calculations. Regarding first the MEP values, there are not significant differences in the values on those five considered atoms of DD1 in the three media and, only the expected tendency in the values due to the electronegativities values are found, that is, O > N > H. But the higher MEP value is observed on N28, as compared with N17 and N21. When the mapped surface for DD1 in gas phase by using the B3LYP/6-311++G** method is graphed from the *GaussView* program in **Figure S4** [40] the different colorations show clearly the nucleophilic and electrophilic regions that presents DD1. Thus, the region on N28 shows higher electronic density and strong red colour indicating nucleophilic sites while on the O15 and N17 weak orange colours are observed and, as a consequence, these places are weak nucleophilic sites. The strong blue colours is observed on the H16 linked to O15 of OH group. This region is a strong electrophilic site because the H16 is the most labile H atom than the other ones. The aromatic H atoms of pyridine, phenyl and imidazole rings shows ligth blue colours due to that these sites are weak electrophilic regions.

When the bond orders (BO), expressed as Wiberg indexes for **DD1** in gas phase and aqueous and DMSO solutions are analyzed from **Table S4** and **Figure S5**, it is observed a low BO value for the H16 atom because this atoms is the most labile while the N21 atom is most strongly linked in DD1 in water than in gas phase and DMSO solution. Then, the BO values for the N17 and N28 atoms are practically the same in the three media. These parameters together with the NPA charges show that the N21 atom of imidazole ring play an important role in the properties of DD1 in the three media.

3.4. NBO and AIM studies

The NBO program allows examining all possible interactions between 'filled' (donor) Lewis-type NBOs and 'empty' (acceptor) non-Lewis NBOs, and estimating their energetic importance by 2nd-order perturbation theory Analysis of Fock Matrix in NBO Basis [36]. These energies values for **DD1** in gas phase and aqueous and DMSO solutions were calculated by using the functional hybrid B3LYP method and two 6-311++G** and 6-31G* basis sets which are presented in **Table S5**. Here, when the calculations were performed with the higher basis set only was obtained for **DD1** in water while for **DD1** in gas phase and in DMSO solution the energies were not obtained because in each medium appear a bond orbital with an occupancy of 2.11250 electrons in gas phase while in DMSO solution the number was 2.10906 electrons. However, when the calculations were performed with the 6-31G* basis set the values of energy were obtained in the three media. Fortunately, when we compare the energy values for water with both sets of bases (7015.67 and 6908.62 kJ/mol for 6-31G* and 6-311++G** basis sets, respectively), few differences between them were found, indicating that little influence has the size of the base set on the energy values. For **DD1** in the three media are observed six different interactions which are, $\pi \rightarrow \pi^*$, $n \rightarrow \sigma^*$, $\sigma \rightarrow LP^*$, $LP \rightarrow LP^*$, $LP \rightarrow \pi^*$ and $\pi^* \rightarrow \pi^*$. The higher energy values are observed in the $\pi \rightarrow \pi^*$, $LP \rightarrow LP^*$ and $\pi^* \rightarrow \pi^*$ transitions carried out from bonding C-C or C-N orbitals to antibonding orbitals and from lone pairs of O and N atoms to C-C or C-N and to lone pairs of H16 atom. These analyses support clearly the presence of intra-molecular O15-H16•••N17 bonds of **DD1** in the three media. A very important result is the high energy values of **DD1** in gas phase and DMSO solution and the low value in water, evidencing that in aqueous solution is most unstable **DD1** due to its higher solvation energy.

The presence of different types of interactions were also studied with the Bader's theory of atoms in molecules (AIM) because this theory use the topological properties to calculate the electron density, $\rho(r)$, the Laplacian values, $\nabla^2\rho(r)$, the eigenvalues ($\lambda 1$, $\lambda 2$, $\lambda 3$) of the Hessian matrix and, the $|\lambda 1|/\lambda 3$ ratio in the bond critical points (BCPs) and ring critical points (RCPs) from the AIM 2000 program [37,38]. Hence, ionic or highly polar covalent interactions or hydrogen bonds interactions are easily predicted when $\lambda 1/\lambda 3 < 1$ and $\nabla^2\rho(r) > 0$ (closed-shell interaction). The resulted of these analyses for **DD1** in gas phase and aqueous and DMSO solutions in the BCPs and Ring RCPs by using B3LYP/6-311++G** calculations can be seen in **Table S6**. Whereas in **Figure S6** is shown the molecular graphic only for **DD1** in gas phase showing the intra-molecular O15-H16•••N17 interaction. The same interaction is also observed in gas phase and in DMSO solution. The new RCP is named RCPN1 while RCP1, RCP2 and RCP3 correspond to the RCP of pyridine (R1), phenyl (R2) and imidazole (R3) rings.•Table S6 shows that the distance between the H16 and N17 atoms that forming those intra-molecular bonds is higher in water than the other ones, as expected because the permittivity of water is higher in this medium (78.355) than the corresponding to DMSO (46.826) and gas (vacuum). Higher parameters are observed in DMSO and lower in water confirming that the stability is higher in DMSO because **DD1** has higher solvation energy in water.

3.5. Frontier orbitals and quantum chemical descriptors

Previous studies performed for **DD1** in the different media have evidenced interesting properties for this new quinoline derivative and, probably its high solvation energy value in aqueous solution could support its use as antiviral drug candidate. For these reasons,

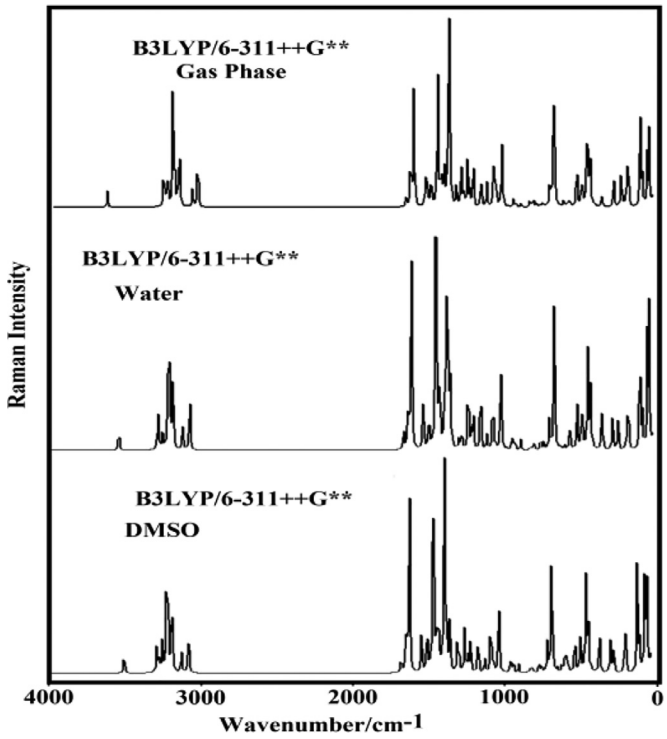

Fig. 5. Experimental Infrared spectra of 5-((1H-imidazol-1-yl)methyl)quinolin-8-ol (**DD1**) in the solid phase compared with the predicted in gas phase and aqueous and DMSO solution by using the hybrid B3LYP/6-311++G** method.

calculations of frontier orbital, gap values and chemical potential (μ), electronegativity (χ), global hardness (η), global softness (S), global electrophilicity index (ω) and global nucleophilicity index (E) descriptors are very important to predict reactivities and behaviours of **DD1** in the three studied media [19-22,51,60-65]. **Table S7** shows those parameters for **DD1** in gas phase and aqueous and DMSO solutions by using the B3LYP/6-311++G** method compared with the hydrochloride form of antiviral adamantadine in water and with both S and R forms of chloroquine in water by using the same level of theory. The differences between HOMO and LUMO, named gap, shows lower values in **DD1** in the three media and, hence, a higher reactivity is expected for **DD1** and, in particular, in DMSO solution while the R form of chloroquine is the less reactive than the other ones. A higher global electrophilicity index (ω) and a lower global nucleophilicity index (E) predicted for **DD1** in DMSO could justify its higher reactivity in this medium. Comparisons of these parameters with reported for antiviral agents in the same medium and with the same basis set suggest that **DD1** could be a very good antiviral drug candidate.

3.6. Vibrational study

The experimental infrared spectra of the title compound **DD1** in the solid state was recorded using reflectance (ATR) mode and its comparison with the corresponding predicted in the gas phase and aqueous and DMSO solutions by using the B3LYP/6-311++G** method are given in Fig. 5. The predicted Raman spectra of **DD1** in the three media can be seen in Fig. 6. Here, the theoretical Raman spectra were corrected from activities to intensities by using recommended equations [44,45]. The optimized structures in the three media present C_1 symmetries and 28 atoms, hence, for this species are expected 78 vibration normal modes. All vibration modes present activity in the infrared and Raman spectra. The scaled quantum mechanical force field (SQMFF) methodology and the Molvib program were used, together with the normal internal coordinates and transferable scaling factors, to calculate the harmonic force fields of **DD1** in the three media at the same level of theory [41-43]. Then, the vibrational assignments of bands observed in the experimental infrared spectrum to the vibration modes were performed considering potential energy distribution (PED) contributions $\geq$ 10 %. In **Table 6** are summarized observed and calculated wavenumbers for **DD1** in gas phase and aqueous solution by using B3LYP/6-311++G** calculations together with the corresponding assignments. In the region of higher wavenumbers the assignments in gas phase are practically the same than in aqueous solution and, only the C2-H7 and C1-H6 stretching modes corresponding to pyridine ring are predicted interchanged in solution in relation to the gas phase. Later, assignments for some groups are discussed below.

The weak IR bands at 2794w, 2750w and 1890w could be attributed to the dimeric species because the calculations were performed in the gas phase to the isolated molecule where the forces packing in the solid phase were not considered. **Figure S7** shows the predicted IR spectra in the three media and the increase in the intensities of some bands in solution.

Assignments O-H group. The OH stretching vibrations are generally observed around 3500–3300 cm^{-1} [63]. This absorption is strongly influenced by the chemical environment, in particular when OH group are involved in the intramolecular or intermolecular hydrogen bond [66-68]. De Freitas et al. [66] reported the OH stretching vibration of the 8-hydroxyquinoline-2-carboxaldehyde isonicotinoylhydrazone at 3396 cm^{-1}. On the other hand, Benković et al. [69] reported the stretching of the OH groups, involved in the intramolecular hydrogen bond with the nitrogen atom of the group C=N, of hydrazones with hydroxyl group in position 2 of phenyl ring at 3142 cm^{-1}. In the present study, the broad and very weak IR band at 3490 cm^{-1} have been assigned to stretching modes of OH involved in the intramolecular hydrogen bond for **DD1** (Figs. 5 and 6). Note that in solution this mode is predicted to lower wavenumbers due to the hydration. In general, the OH in-plane deformation vibration for phenols lies in the region 1440-1260 cm^{-1} [70], Arunagiri et al. [71] reported the in-plane deformation vibrations of two OH at 1242 and 1220 cm^{-1}.

In this work, the observed in-plane deformation vibrations of OH for **DD1** in gas phase and aqueous solution are predicted at 1180 and 1172 cm^{-1}, respectively while the out-of-plane deformation or torsion mode of OH for **DD1** in gas phase is predicted at 569 cm^{-1} and, in solution it is predicted shifted at 492 cm^{-1} due to the hydration, as observed in similar compounds containing this group [58-65].

Assignments C-H groups. The C-H stretching vibrations of aromatic rings give rise to bands in the region 3100–3000 cm^{-1} in aromatic compounds [55-58,60,72]. For the title molecule, a series of infrared absorptions between 3168 and 2989 cm^{-1} were assigned as CH stretching modes of the quinolone, imidazole and benzotriazole rings. The C-H in-plane deformation vibrations are observed in the region 1500–1058 cm^{-1} and are usually of medium to weak intensity [55-58,60,65,72]. In the present work, the bands due to C-H in-plane bending vibration interact somewhat with C–C stretching vibrations, hence, they are assigned to IR bands between 1472 and 1054 cm^{-1}. The out-of-plane CH deformations are predicted and assigned between 999 and 715 cm^{-1} [55-58,60,65,72]. The assignments of these vibration modes in solution are slightly different from those predicted in gas phase, as can be seen in Table 6. In our case, the strong IR bands at 823, 791 and 696 cm^{-1} together with the band of medium intensity at 927 cm^{-1} are assigned to CH out-of-plane deformation vibrations.

Assignments CH_2 groups. These vibration modes are influenced by the medium because in solution are predicted at higher wavenumbers than in gas phase. Thus, the anti-symmetric and symmetric stretching modes are predicted in gas phase at 2943

Table 6
Observed and calculated wavenumbers (cm^{-1}) and assignments for 5-((1H-imidazol-1-yl)methyl)quinolin-8-ol (**DD1**) in gas phase and aqueous solution by using the B3LYP/6-311++G(d,p) Method.

Exp[a] IR	DD1[a] GAS Int[b]	SQM[c]	Assignments[a]	PCM SQM[c]	Assignments[a]
3490vw	113.8	3480	νO15-H16	3409	νO15-H16
3168w	2.5	3125	νC22-H25	3162	νC22-H25
3120sh	1.1	3115	νC23-H26	3157	νC23-H26
3100sh	4.6	3101	νC24-H27	3133	νC24-H27
3092w	7.3	3068	νC2-H7	3100	νC1-H6
3080sh	4.6	3066	νC11-H13	3091	νC11-H13
3044vw	5.0	3054	νC1-H6	3087	νC2-H7
	10.7	3032	νC12-H14	3070	νC12-H14
2989w	16.7	3024	νC5-H10	3066	νC5-H10
2969w	10.0	2943	$\nu_a CH_2$	3004	$\nu_a CH_2$
2913w	30.5	2911	$\nu_s CH_2$	2962	$\nu_s CH_2$
1687w	14.4	1610	νC9-C11	1624	νC9-C11,νC8-C12
1616w	6.1	1582	νC1-C2,νC8-C12	1597	νC1-C2
1568m	37.9	1563	νC5-N17	1578	νC5-N17
1500s	134.8	1488	νC1-C5	1509	νC23-N21
	0.3	1481	νC22-C24	1502	νC22-C24
1472s	60.0	1474	νC23-N28,βC23-H26	1500	νC1-C5,βC1-H6
1448m	104.9	1457	νC4-C9	1465	βC5-H10,νC4-C9
1436sh	24.7	1435	δCH_2	1454	δCH_2
1409m	14.5	1407	βC5-H10	1421	$wagCH_2$,βC5-H10
	15.0	1394	βC2-H7,νC3-C8	1412	$wagCH_2$
1388m	24.4	1387	$wagCH_2$	1409	βC2-H7
1368m	49.6	1356	νC3-C4,νC8-C12	1367	νC3-C4
1345m	26.8	1332	νC3-C4	1343	νC5-N17,νC3-C4
1333sh	2.5	1325	νC23-N28	1333	νC23-N28
1297sh	20.0	1296	νC23-N21	1330	νC23-N28,νC23-N21
1269s	68.9	1266	βR_1(A2)	1278	βC24-H27
1269s	80.2	1264	βC24-H27	1265	βR_1(A2)
1237vs	10.7	1245	βC12-H14	1259	βC12-H14
1237vs	121.6	1219	νC4-N17,νC9-O15	1226	βC23-H26,νC18-N21
1217sh	61.9	1211	νC18-N21	1214	νC2-C3, νC3-C8,νC4-N17
1205sh	34.2	1191	ρCH_2	1204	ρCH_2
1181m	11.0	1180	δO15-H16,νC2-C3	1172	δO15-H16
1150m	3.4	1143	βC11-H13	1149	βC1-H6
1142sh	2.8	1137	βC1-H6,νC11-C12,νC8-C18	1137	νC11-C12,βC11-H13,νC9-O15 ,νC8-C18
1102sh	22.9	1100	νC24-N28	1101	νC24-N28
1074s	2.5	1068	βR_1(A1)	1067	βC22-H25
1054sh	40.3	1058	βC22-H25	1062	βR_1(A1)
1030m	1.5	1044	νC1-C5,βR_1(A1)	1056	νC1-C5
1010sh	5.0	1017	νC22-N21	1019	βR_1(A3),νC22-N21
	18.3	1001	νC1-C5	1005	νC1-C5
986sh	0.4	989	γC1-H6	999	γC1-H6
951sh	1.5	952	γC5-H10,γC2-H7	967	γC5-H10
927m	0.8	945	γC12-H14	953	γC12-H14
911sh	2.9	909	βR_2(A3)	912	βR_2(A3)
871sh	8.6	882	τwCH_2	891	τwCH_2
859sh	1.9	854	γC24-H27	850	γC11-H13
843sh	21.6	841	γC11-H13	842	γC24-H27
823s	4.6	827	βR_3(A1)	827	γC23-H26
823s	25.5	814	γC23-H26	826	βR_3(A1)
791s	26.6	805	τR_1(A1), γC2-H7	816	γC2-H7
752sh	20.9	779	τR_1(A2)	778	τR_1(A2),τR_1(A1)
728vs	3.3	765	τR_1(A1), τR_1(A2)	760	τR_1(A1), βR_1(A2)
728vs	10.1	725	τR_1(A1), νC18-N21	732	γC22-H25
696s	34.4	715	γC22-H25	728	τR_1(A1), νC18-N21
696s	25.6	696	βR_2(A1)	695	βR_2(A1)
660s	15.6	651	τR_1(A3)	653	τR_1(A3)
640m	33.8	632	τR_1(A1)	629	τR_1(A1), τR_1(A2)
620m	65.1	603	τR_2(A3)	602	τR_2(A3)
	6.5	593	γC9-O15	595	γC9-O15
577w	1.3	570	βR_2(A1), γC9-O15	567	βR_2(A1), γC9-O15
	7.7	569	τO15-C9	535	βR_3(A1)
545sh	0.6	537	βR_2(A2)	504	βR_2(A2)
	17.6	507	βR_2(A2)	492	τO15-C9
493m	0.6	492	βR_3(A2)	490	βR_3(A2)
465w	0.2	459	τR_2(A2)	463	τR_2(A2)

(*continued on next page*)

Table 6 (*continued*)

Exp[a]	DD1[a]				
	GAS			PCM	
IR	Int[b]	SQM[c]	Assignments[a]	SQM[c]	Assignments[a]
453sh	1.9	413	τR_3(A1)	413	τR_3(A1)
	0.9	353	τR_2(A2), τR_2(A1)	360	τR_2(A2), τR_2(A1)
	1.5	312	βN21-C18	330	βN21-C18
	3.2	280	γC9-O15	277	βN21-C18,βR_2(A2)
	2.4	272	βR_3(A2), βC8-C18	269	γC9-O15
	2.2	192	βC8-C18	196	βC8-C18
	2.3	177	ButC3-C4,γN21-C18	177	ButC3-C4,γN21-C18
	0.1	148	τR_3(A2)	146	τR_3(A2)
	0.6	132	τR_2(A1)	133	τR_2(A1)
	1.3	50	γC8-C18,δC8C18N21	48	γC8-C18,δC8C18N21
	0.3	36	τC18-N21	41	τC18-N21
	2.9	33	τC18-C8	25	τC18-C8

Abbreviations: ν, stretching; β, deformation in the plane; γ, deformation out of plane; wag, wagging; τ, torsion; β_R, deformation ring τ_R, torsion ring; ρ, rocking; τw, twisting; δ, deformation; a, antisymmetric; s, symmetric; (A_1), Ring 1; (A_2), Ring 2; (A_3), Ring 3;

[a] This work,

[b] Intensities in KM/Mole;

[c] From scaled quantum mechanics force field.

and 2911 cm^{-1} while in solution are predicted at 3004 and 2962 cm^{-1}, respectively. The remaining deformation, wagging, rocking and twisting modes are observed at higher wavenumbers in aqueous solution. Probably, the proximity of this group with the imidazole ring justifies these differences.

Assignments skeletal groups. The C=N stretching vibration is reported at 1613 cm^{-1} by Sheeja et al. [72]. Here, the C5=N17 and C23=N28 stretching modes are predicted in gas phase at 1563 and 1474 cm^{-1} while in solution at 1578 and 1333 cm^{-1}. Note that the C23=N28 stretching mode in solution is predicted coupled with the C23-N21 stretching mode. The aromatic C=C-C stretching vibrations of aromatic ring are very much important and occur in the region 1200-1650 cm^{-1} [19-22,55-58,60]. In DD1, the IR bands in the range 1687-1457 cm^{-1} are assigned to C=C stretching mode in aromatic rings while the C-C stretching modes are predicted by SQM calculation between 1367 and 1001 cm^{-1}. Then, these modes are assigned in those regions, as predicted by calculations. Here, the C18-N21 stretching modes in both media are predicted couples with one of torsion modes of pyridine ring between 728 and 725 cm^{-1}, that is, practically in the same region. Hence, we can see that that mode is not influenced by the medium. The assignments of other groups in the 360 and 25 cm^{-1} region such as, deformations and torsions of three rings were not performed because the infrared spectrum was recorded only until 400 cm^{-1}.

3.7. Force fields

Calculations of harmonic force fields for **DD1** in the three media by using the B3LYP/6-311++G** method have allowed to compute the scaled force constants which are very important parameters that explain the forces of different bonds. Thus, these constants are obtained when the harmonic force fields are transformed from Cartesian coordinates to normal internal coordinates with the SQMFF methodology and the Molvib program [41-43]. The results for **DD1** in the three media are presented in **Table 7**. The $f(\nu C\text{-}H)_{R1}$ force constants corresponding to the C-H bonds of different rings were separate in R1 (pyridine), R2 (contain the OH group) and R3 (imidazole) because they have different behaviours and environments in the different media. Thus, first analyzing the $f(\nu O\text{-}H)$ force constants we observed that in DMSO solution **DD1** present the lower force constant while in gas phase the value is higher. This observation is in agreement with the lower frequency

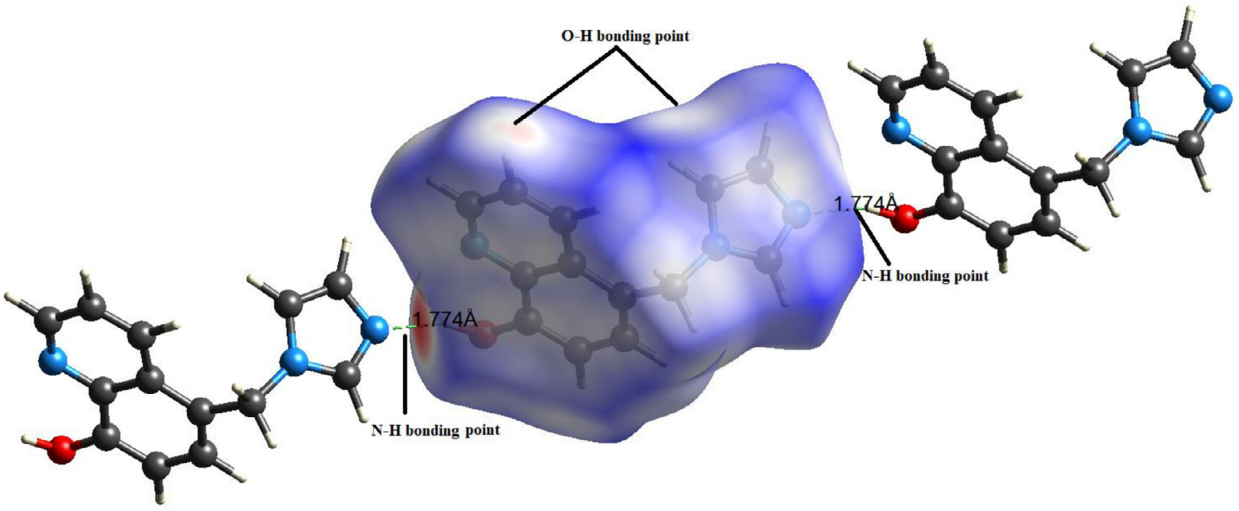

Fig. 6. Predicted Raman spectrum of 5-((1H-imidazol-1-yl)methyl)quinolin-8-ol (**DD1**) in gas phase and aqueous and DMSO solution by using the hybrid B3LYP/6-311++G** method.

Table 7
Scaled internal force constants of 5-((1H-imidazol-1-yl)methyl)quinolin-8-ol (**DD1**) in gas phase and aqueous and DMSO solutions by using the B3LYP/6-311++G** method.

Force constant	B3LYP/6-311++G** method DD1[a] GAS	Water	DMSO
$f(\nu O\text{-}H)$	6.77	6.49	6.32
$f(\nu C\text{-}O)$	6.22	5.46	6.47
$f(\nu C\text{-}H)_{R1}$	5.09	5.22	5.20
$f(\nu C\text{-}H)_{R2}$	5.10	5.20	5.19
$f(\nu C\text{-}H)_{R3}$	5.30	5.43	5.39
$f(\nu C{=}N)_{R1}$	7.82	7.86	7.91
$f(\nu C{=}N)_{R3}$	7.66	7.59	7.71
$f(\nu CH_2)$	4.73	4.90	4.89
$f(\delta CH_2)$	0.78	0.79	0.79
$f(\delta OH)$	0.83	0.82	0.87

Units are mdyn Å^{-1} for stretching and mdyn Å rad^{-2} for angle deformations
[a] This work

predicted for this bond in DMSO (3409 cm^{-1}) while in water the value increase to 3480 cm^{-1}. On the contrary, when the $f(\nu C\text{-}O)$ force constants are evaluate we observed that in DMSO solution it has a higher value and, it cannot be explained by the frequencies of stretching modes because in both solutions these modes are coupled. An explanation could be due to higher value of $f(\nu O\text{-}H)$ force constant and, hence, to decreasing in the corresponding the $f(\nu C\text{-}O)$ force constant.

When the $f(\nu C\text{-}H)_{R3}$ force constants are analyzed, for the ring R3 are observed the higher values in the three media and, these observations are related to the lower $f(\nu C{=}N)_{R3}$ force constants values evidenced for this ring. Moreover, the MEP value for the N28 atom and the NPA and BO predicted for the N21 atom of R3 ring and, in addition, to its higher electron density, this ring R3 play a very important role in the properties of **DD1** in the three media. Thus, due to the proximity of CH_2 group to ring R3 the stretching modes are influenced by the medium because in solution are observed higher force constants values than in gas phase. However, the deformations of those groups practically are practically similar in the three media.

3.8. Ultraviolet-Visible spectrum

The experimental ultraviolet-visible spectrum of **DD1** in DMSO solution recorded between 200 and 400 nm region can be seen in **Figure S8** compared with the corresponding predicted in aqueous and DMSO solutions by using Time-dependent DFT calculations (TD-DFT) with the hybrid B3LYP/6-311++G** method. In the experimental spectrum we observed a set of intense bands in the higher wavelengths region where the enveloping line presents a maximum at 238 nm and another less intense and wide band at 328 nm. In the predicted electronic spectrum in aqueous solution are also observed two bands, the most intense at 234.7 and te other one at 344.2 nm while in DMSO the positions of these two bands increase respectively at 236.6 and 346.2 nm. The presence of C=C, C=N and lone pairs of N and O atoms justify the presence of those two bands observed in the electronic spectra of **DD1** in the three media which are assigned to $\pi \rightarrow \pi^*$, $LP \rightarrow LP^*$ and $\pi^* \rightarrow \pi^*$ transitions because these present higher energies values, according to NBO calculations.

3.9. ^{1}H- and ^{13}C-NMR spectra analysis

The experimental ^{1}H- and ^{13}C -NMR spectra of **DD1** were obtained by using TMS as an internal standard and DMSO-d_6 as solvent (**Figs. S9** and **S10**). In Tables 8 and 9 are shown the experimental chemical shifts of protons and C atoms compared with

Table 8
Results of the binding affinity and RMSD values of different poses in COVID-19/6Y84 inhibitor of **DD1**.

Modes	Affinity (kcal/mol)	rmsdl.b.	rmsdu.b.
1	-7.2	0.000	0.000
2	-6.9	1.620	3.413
3	-6.7	3.642	5.463
4	-6.5	7.963	9.477
5	-6.5	1.560	2.830
6	-6.4	5.758	7.446
7	-6.3	9.830	11.517
8	-6.3	4.190	5.324
9	-6.2	2.843	5.654
10	-6.1	15.600	17.436

Inhibition Constant: 5.27669 μM
Number of Hydrogen bonding: 1 active bonding

Table 9
Results of the binding affinity and RMSD values of different poses in COVID-19/6WCF inhibitor of **DD1**.

Modes	Affinity (kcal/mol)	rmsdl.b.	rmsdu.b.
1	-6.2	0.000	0.000
2	-6.1	14.750	15.700
3	-6.0	14.379	15.520
4	-5.9	22.551	24.206
5	-5.8	14.275	15.767
6	-5.8	24.802	25.867
7	-5.8	22.076	23.739
8	-5.7	7.108	8.948
9	-5.7	13.539	14.413
10	-5.6	19.175	20.321

Inhibition Constant: 28.5343 μM
Number of Hydrogen bonding: 4 non-active bonding

the corresponding predicted by using Gauge-Independent Atomic Orbital (GIAO) method [46] with the hybrid B3LYP/6-311++G** method. The ^{1}H-NMR chemical shifts of H-19 and H-20 protons of the methylene group (CH_2) of **DD1** appear as a singlet at 5.56 ppm, respectively. The chemical shifts of H-15 and H-25 protons of quinoline appear as a triplet and doublet at 7.59 and 7.06 ppm. These chemical shifts are relatively well reproduced with deviations less than 0.57-0.47 ppm compared to the observed ones. The chemical shifts of H-27 proton of quinoline appear as a doublet at 7.36 ppm for **DD1**. The chemical shifts of H-11 and H-23 protons appear as two doublets of doublets at 8.53, 8.85 ppm. The observed chemical shifts of the hydroxy (H-2) proton of **DD1** appear as singlet at 9.93 ppm. The chemical shifts of the protons of imidazole ring in **DD1** appear as a singlet and two doublets at 7.75, 6.84 and 7.10 ppm. Also, reasonable correlations were found for the C atoms with RMSD values between 5.57 and 5.34 ppm. The ^{13}C-NMR chemical shifts of the C-12 (-C-OH) of **DD1** are observed at 154.01 ppm. The signals observed at 148.54 ppm are attributed to the C-22 carbon (C=N) of the quinoline. The C-10, C-14, C24 and C-26 carbon chemical shifts of the title compound occurred in the range of 111.01-132.86 ppm. The signals at 119.89, 128.91 and 139.13 ppm in ^{13}C NMR spectrum of **DD1** are clearly assigned for three carbons of imidazole ring. The C-18 carbon chemical shift of the methylene group (CH_2) of **DD1** is obtained at 46.88 ppm.

3.10. ESI-MS spectra analysis

The ESI-MS spectra of **DD1** show molecular ion peaks with m/z values 226.1. The peaks correspond to the molecular weight $[M+H]^+$ of **DD1**. The m/z value at 248.4 is assigned to the sodiated molecular ion peak $[M+Na]^+$ for **DD1** (**Fig. S11**). These values are in good agreement with the proposed composition for the title compound.

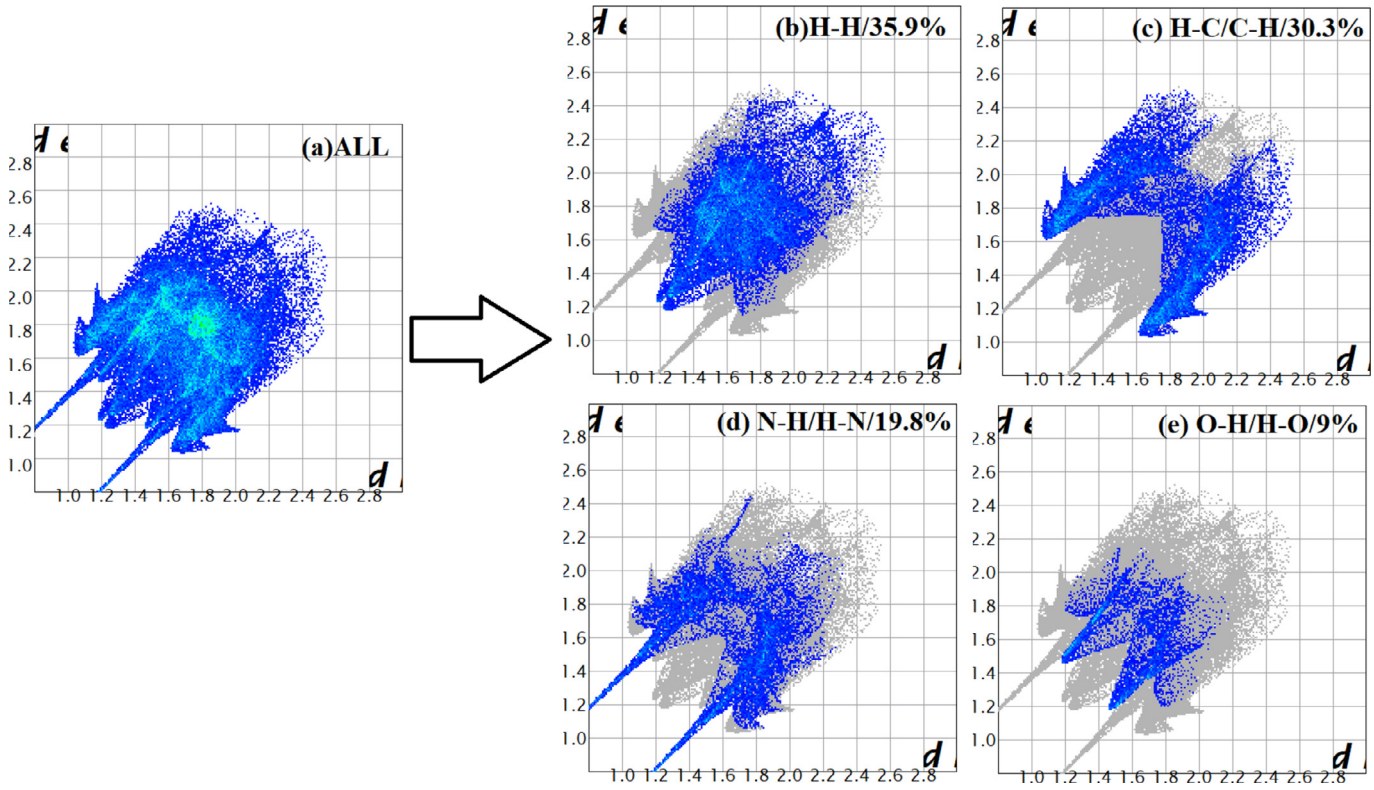

Fig. 7. d_{norm} mapped on Hirshfeld surface for visualizing the intercontacts of **DD1**.

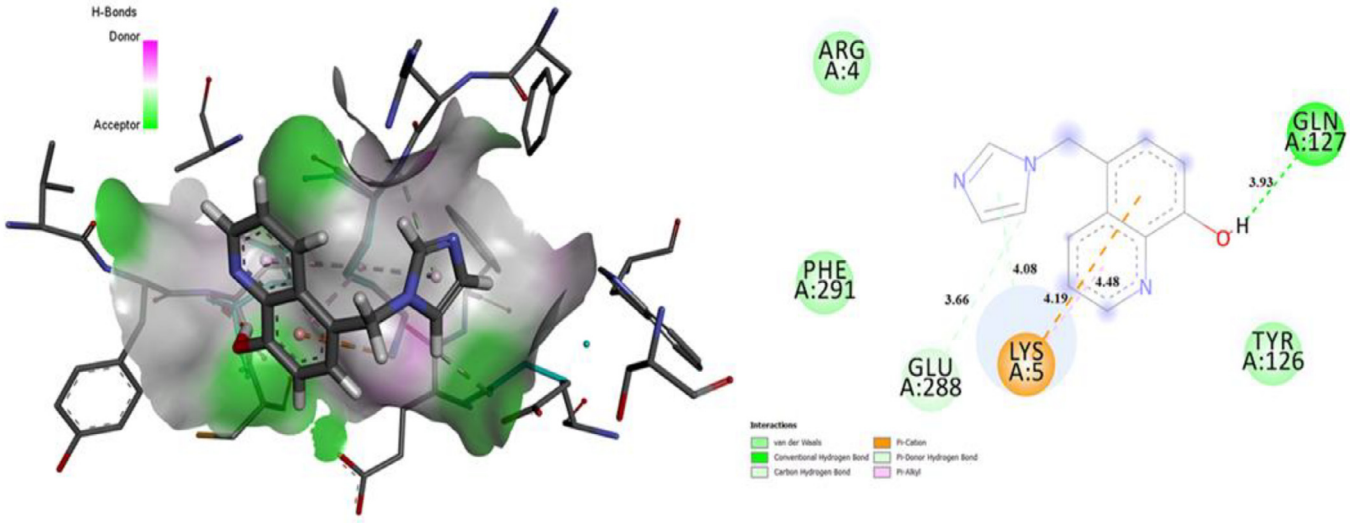

Fig. 8. Finger plots of compound **DD1**.

3.11. Hirshfeld surface analysis

In this section, the Hirshfeld surface analysis of the **DD1** molecule were carried out with the help of Crystal Explorer 3.1 program [73]. Thanks to this analysis, the locations of the possible hydrogen bonds in the crystal structure and the packaging model can be easily seen and there are three type color (red, blue and white) in the visualization of intermolecular interactions [74,75]. For analysis, cif* (Crystallographic Information File) of the compounds are used. The d_{norm} values of compounds were obtained as -0.6660 to 1.1031 a.u. for **DD1**. Here, the negative values represent red, positive values represent blue color and d_{norm} mapped on Hirshfeld surfaces were shown as in Fig. 7.

In Fig. 7, the dark red points focused on N, O, H atoms, here O-H…N interaction was observed with 1.774 Å, additionally in this figure O-H interaction point was shown.

Secondly, the 2D (two-dimensional) fingerprint plots with their relative contributions to the Hirshfeld surfaces we indicated in Fig. 8a-e for **DD1**. As seen from the **Fig. 8**, the most important interactions were determined with H···H (35.9%), C···H/H···C (30.3%), N···H/H···N (19.8%) and O···H/H···O (9%) contributions.

3.12. Molecular Docking Studies

In this section, the molecular docking analysis of 5-((1H-imidazol-1-yl) methyl) quinolin-8-ol (**DD1**) ligand with COVID-

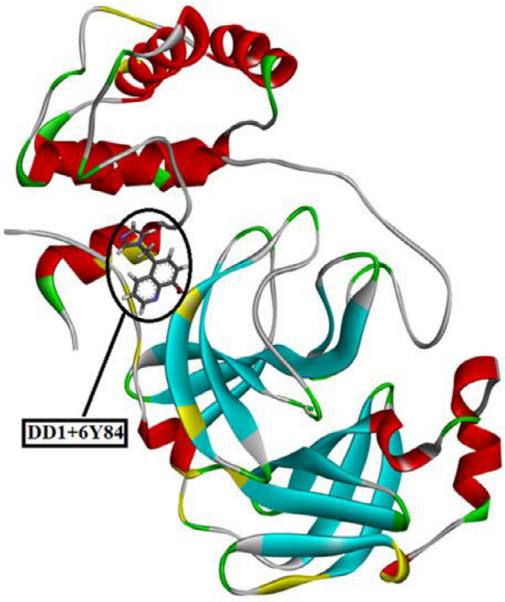

Fig. 9. The molecular docking results of the **DD1** compound with 6Y84 protein, surfaces around ligand (a) and 2D forms (b).

19/6WCF and COVID-19/6Y84 receptors were performed. For structure-based drug design, the molecular docking is very crucial [76,77]. Here as ligand, **DD1** molecule was optimized with B3LYP/6-311++G(d,p) and was recorded PDB-Protein Data Bank format. Later, the two target proteins were determined with the help of literature and PDB structures of receptors were downloaded from the Protein Data Bank [78]. The specific treatment for COVID-19 is not available to date, so by researchers many antiretroviral drugs against COVID-19 were reported and was offered such as ritonavir, lopinavir, oseltamivir, remdesivir, chloroquine and hydroxychloroquine [79]. Since some of these structures are quinoline derivative, we decided to do docking analysis of **DD1** that we can recommend against COVID-19. In the receptors water molecules and co-factors were removed. Both ligands and receptors were prepared and recorded as PDBQT formats with Discover Studio Visualizer 4.0 (DSV 4.0) software [80]. The molecular docking computations were performed with AutoDock Vina program [50].

Let's first look at the interactions between **DD1** ligand and the 6Y84 receptor. 6Y84 is the COVID-19 main protease with unliganded active site. SARS-CoV-2 main protease has a vital role in the processing of polyprotein that is translated from viral RNA, and the protease is considered as key for viral survival and growth [81]. The active sites of PDB:6Y84 were determined as ARG298, ASP295, ASP263, THR224, PHE223, GLN127, SER113, LYS97, ARG76, LEU75, GLN74, ASN65, HIS64, MET17, GLY15, PHE8 and MET6 and according to these active residues the grid boxes were taken as centre_x=8.562, centre_y=1.084, centre_z=5.876, size_x=76, size_y=72, size_z=80, spacing=0.442. For these interactions, the docking results were given in Table 8, also between **DD1**-6Y84 docking mechanism as 2D and 3D were shown in Fig. 9.

In addition, the positions of **DD1** within the receptor (6Y84) were shown in Fig. 10. The best binding was determined with -7.2 (kcal/mol) energy between **DD1** ligand and 6Y84 receptor according to the affinity energies with two hydrogen bonding. But one active hydrogen bonding was observed GLN127 active residue and H2 atom with 2.33 Å bond distance as seen Fig. 9. Furthermore, from the Fig. 9 van der Waals, π-cation, π-donor hydrogen bond and π-alkyl interactions could be easily seen. At the last of the tables, the obtained inhibition constants and the number of hydrogen bonding for **DD1**-6Y84 interactions were given.

Secondly, the molecular docking mechanism between **DD1** ligands and the 6WCF receptor was investigated and evaluated. 6WCF is Crystal Structure of ADP ribose phosphatase of NSP3 from SARS-CoV-2 in complex with MES [82]. The active sites of PDB:6WCF were detected as PHE132, ILE131, GLY130, ALA129, ASN72, THR71, SER128, LYS55, ALA52, GLY51, GLY47, GLY46, LYS44, ASN40, and ALA38. As mentioned before, the grid parameters were determined to include the active region as follows : centre_x=-4.969, centre_y=8.796, centre_z=-5.972, size_x=62, size_y=84, size_z=42, spacing=0.375. The same grids were used in both ligands and the docking scores were tabulated in Table 9 and additionally between **DD1**-6WCF docking mechanism were indicated as 2D and 3D in Fig. 11.

Furthermore, the positions of **DD1** within the 6WCF receptor were indicated in Fig. 11. As seen from the Table 9, the best binding was determined with -6.2 (kcal/mol) energy between **DD1** ligand and 6WCF receptor with two active hydrogen bonding (Fig. 10).

The bond distances between ALA129-N5 and SER128-N6 were determined as 2.35 and 2.70 Å, respectively. Additionally, from the

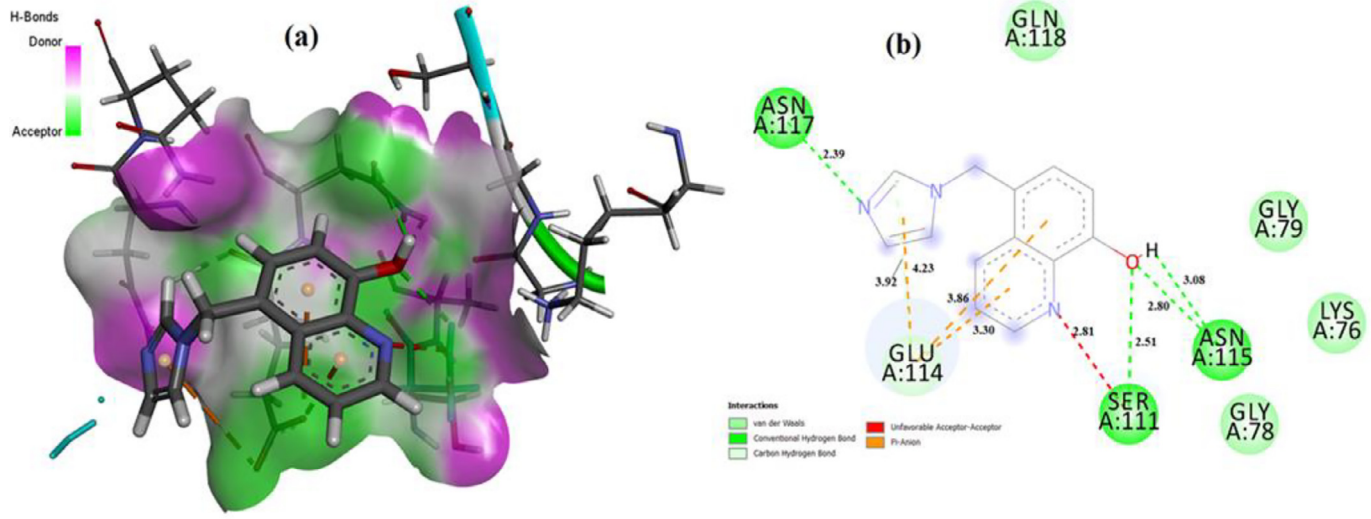

Fig. 10. The molecular docking positions of the **DD1** compound within 6Y84 protein.

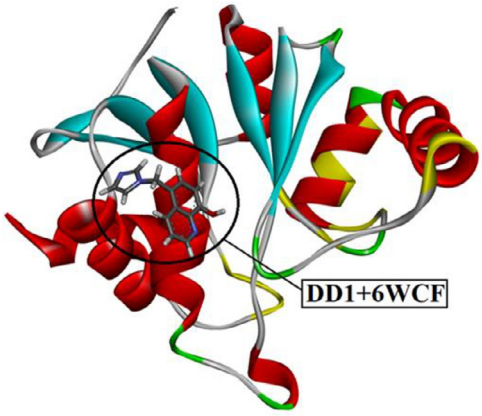

Fig. 11. The molecular docking results of the **DD1** compound with 6WCF protein, surfaces around ligand (a) and 2D forms (b).

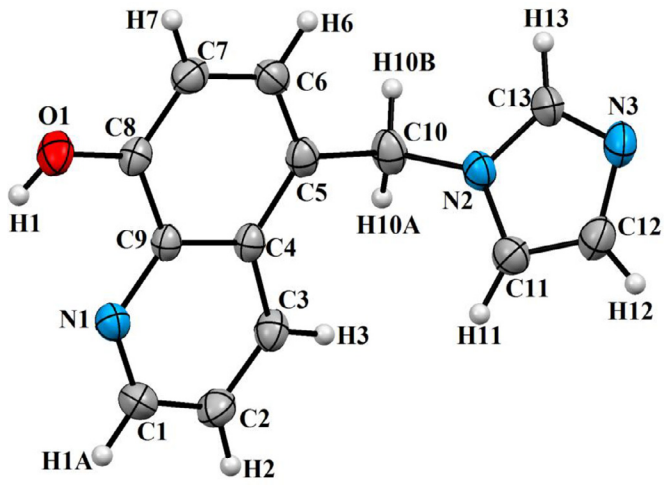

Fig. 12. The molecular docking positions of **DD1** within 6WCF protein.

Fig. 12 van der Waals, carbon hydrogen bond, π-π-T shaped and π-alkyl interactions could be easily observed and at the last of the tables, the inhibition constants and the number of hydrogen bonding for **DD1**-6WCF interactions were given. The inhibition constants were computed with the help of Ki=exp(ΔG/RT) equation, where, ΔG, R and T are the docking binding energy, gas constant (1.9872036 $\times$ 10^{-3} kcal/mol) and room temperature (298.15 K), respectively. From the molecular docking results, it is concluded that **DD1** molecule can be considered as potential agent against COVID-19/6Y84-6WCF receptors.

4. Conclusions

In this work, a new chloroquine analogue, 5-((1H-imidazol-1-yl)methyl)quinolin-8-ol (**DD1**) with potential antiviral agent against COVID-19/6Y84-6WCF receptors has been synthesized and characterized by FT-IR, ^{1}H-NMR, ^{13}C-NMR, UV-visible, ESI-MS and single-crystal X-ray diffraction. Good correlations between experimental and theoretical infrared spectra, ^{1}H and ^{13}C NMR chemical shifts and electronic spectrum in DMSO were obtained by using the hybrid B3LYP/6-311++G(d,p) method. Structural, electronic, topological and vibrational properties were performed in gas phase, aqueous and DMSO solutions. Higher solvation energy was observed in aqueous solution than in DMSO showing higher solvation energy in aqueous solution than antiviral brincidofovir and chloroquine. Behaviors of atomic Mulliken, NPA charges and topological properties suggest that imidazole ring play a very important role in the properties of **DD1**. NBO and AIM analyses support the intra-molecular O15-H16•••N17 bonds of **DD1** in the three media evidencing higher stability in DMSO solution. The low gap values suggest a higher reactivity of **DD1** in DMSO solution justified probably by the higher electrophilicity and low nucleophilicity. Comparisons of gap with antiviral agents suggest that **DD1** could be a very good antiviral drug candidate. Here, the complete vibrational assignments of **DD1** in gas phase and aqueous solution are reported together with the scaled force constants. Hirshfeld surface analysis was performed to observe better intermolecular interactions in the crystal packing of **DD1**. Finally, molecular docking results have shown that the compound can be considered as a potential agent against COVID-19 / 6Y84-6WCF receptors.

Credit Author Statement

Dhaybia Douche: Methodology, Investigation. **Yusuf Sert**: Software, Writing - Original Draft. **Silvia A. Brandán:** Software, Validation, Writing- Reviewing and Editing. **Ameed Ahmed Kawther**: Conceptualization, Methodology. **Bayram Bilmez**: Investigation, Resources. **Necmi Dege**: X-ray data, Validation, Collected the data. **Ahmed El Louzi**: Investigation, Resources. **Khalid Bougrin**: Investigation, Resources. **Khalid Karrouchi**: Writing - Original Draft, Writing - Review & Editing. **Banacer Himmi**: Supervision.

Declaration of Competing Interest

The authors declare that they have no known competing financial interests or personal relationships that could have appeared to influence the work reported in this paper.

Acknowledgements

This work is supported by UM5R and Ondokuz Mayıs University (award No. PYO.FEN.1906.19.001) as well as grants from CIUNT Project N° 26/D608 (Consejo de Investigaciones, Universidad Nacional de Tucumán).

Supplementary materials

Supplementary material associated with this article can be found, in the online version, at doi:10.1016/j.molstruc.2021.130005.

References

[1] X.M. Chu, C. Wang, W. Liu, L.L. Liang, K.K. Gong, C.Y. Zhao, K.L. Sun, Quinoline and quinolone dimers and their biological activities: an overview, Eur. J. Med. Chem. 161 (2019) 101–117.
[2] L. Senerovic, D. Opsenica, I. Moric, I. Aleksic, M. Spasić, B. Vasiljevic, Quinolines and Quinolones as Antibacterial, Antifungal, Anti-virulence, Antiviral and Anti-parasitic Agents, Adv. Exp. Med. Biol. (2019) 1–33.
[3] S.M.A. Hussaini, Therapeutic significance of quinolines: a patent review (2013-2015), Expert Opin. Ther. Pat. 26 (2016) 1201–1221.
[4] S.Kitane B.Himmi, J.P.Joly A.Eddaif, M.Soufiaoui F.Hlimi, A. Sebban, Synthesis of novel 5, 7-disubstituted 8-hydroxyquinolines, J. Heterocycl. Chem. 45 (2008) 1023–1026.
[5] D. Douche, H. Elmsellem, E.H. Anouar, L. Guo, B. Hafez, B. Tüzün, A.El Louzi, K. Bougrin, K. Karrouchi, B. Himmi, Anti-corrosion performance of 8-hydroxyquinoline derivatives for mild steel in acidic medium: Gravimetric, electrochemical, DFT and molecular dynamics simulation investigations, J. Mol. Liq. (2020) 113042.
[6] Y. Bouzian, K. Karrouchi, Y. Sert, C.H. Lai, L. Mahi, N.H. Ahabchane, A. Talbaoui, J.T. Mague, E.M. Essassi, Synthesis, spectroscopic characterization, crystal structure, DFT, molecular docking and in vitro antibacterial potential of novel quinoline derivatives, J. Mol. Struct. 1209 (2020) 127940.
[7] P. Wadhwa, P. Jain, S. Rudrawar, H.R. Jadhav, Quinoline, coumarin and other heterocyclic analogs based HIV-1 integrase inhibitors, Curr. Drug Discov. Technol. 15 (2018) 2–19.
[8] G. Barbosa-Lima, A.M. Moraes, A.D.S. Araújo, E.T. da Silva, C.S. de Freitas, Y.R. Vieira, T.M.L. Souza, 2, 8-bis (trifluoromethyl) quinoline analogs show improved anti-Zika virus activity, compared to mefloquine, Eur. J. Med. Chem. 127 (2017) 334–340.

[9] D. Al-Saad, M.G. Memeo, P. Quadrelli, # Nitrosocarbonyls 1: Antiviral Activity of N-(4-Hydroxycyclohex-2-en-1-yl) quinoline-2-carboxamide against the Influenza A Virus H1N1, Scientific World J 2014 (2014) 1–10.

[10] I. Briguglio, R. Loddo, E. Laurini, M. Fermeglia, S. Piras, P. Corona, C. Ibba, Synthesis, cytotoxicity and antiviral evaluation of new series of imidazo [4, 5-g] quinoline and pyrido [2, 3-g] quinoxalinone derivatives, Eur. J. Med. Chem. 105 (2015) 63–79.

[11] C. De la Guardia, D.E. Stephens, H.T. Dang, M. Quijada, O.V. Larionov, R. Lleonart, Antiviral activity of novel quinoline derivatives against dengue virus serotype 2, Molecules 23 (2018) 672.

[12] R. Loddo, I. Briguglio, P. Corona, S. Piras, M. Loriga, G. Paglietti, P. Farci, Synthesis and antiviral activity of new phenylimidazopyridines and N-benzylidenequinolinamines derived by molecular simplification of phenylimidazo [4, 5-g] quinolines, Eur. J. Med. Chem. 84 (2014) 8–16.

[13] B.P. Moore, D.H. Chung, D.S. Matharu, J.E. Golden, C. Maddox, L. Rasmussen, E.L. White, F. Jia, T.E. Prisinzano, J. Aube, C.B. Jonsson, W.E. Severson*, (S)-N-(2, 5-dimethylphenyl)-1-(quinoline-8-ylsulfonyl) pyrrolidine-2-carboxamide as a small molecule inhibitor probe for the study of respiratory syncytial virus infection, J. Med. Chem. 55 (2012) 8582–8587.

[14] M. Wang, R. Cao, L. Zhang, Remdesivir and chloroquine effectively inhibit the recently emerged novel coronavirus (2019-nCoV) in vitro, Cell Research 30 (2020) 269–271.

[15] J. Gao, Z. Tian, X. Yang, Breakthrough: chloroquine phosphate has shown apparent efficacy in treatment of COVID-19 associated pneumonia in clinical studies, Biosci Trends 14 (2020) 72–73.

[16] J. Liu, R. Cao, M. Xu, X. Wang, H. Zhang, H. Hu, et al., Hydroxychloroquine, a less toxic derivative of chloroquine, is effective in inhibiting SARS-CoV-2 infection in vitro, Cell Discov 6 (2020) 16.

[17] C. Biot, W. Daher, N. Chavain, T. Fandeur, J. Khalife, D. Dive, et al., Design and synthesis of hydroxyferroquine derivatives with antimalarial and antiviral activities, J. Med. Chem. 49 (2006) 2845–2849.

[18] P. Gautret, J.C. Lagier, P. Parola, V.T. Hoang, L. Meddeb, M. Mailhe, et al., Hydroxychloroquine and azithromycin as a treatment of COVID-19: results of an open-label non-randomized clinical trial, Int. J. Antimicrob. Agents. (2020).

[19] K. Karrouchi, S.A. Brandán, Y. Sert, H. El-marzouqi, S. Radi, M. Ferbinteanu, M.E.A. Faouzi, Y. Garcia, M. Ansar, Synthesis, X-ray structure, Vibrational spectroscopy, DFT investigation and biological evaluation studies of (*E*)-*N*'-(4-(dimethylamino)benzylidene)-5-methyl-1H-pyrazole-3-carbohydrazide, J. Mol. Struct. 1219 (2020) 128541.

[20] K. Karrouchi, S.A. Brandán, Y. Sert, M.El Karbane, S. Radi, M. Ferbinteanu, Y. Garcia, M. Ansar, Synthesis, structural, molecular docking and spectroscopic studies of (E)-N'-(4-methoxybenzylidene)-5-methyl-1H-pyrazole-3-carbohydrazide, J. Mol. Struct. 1225 (2020) 129072.

[21] F. El Kalai, K. Karrouchi, C. Baydere, S. Daoui, M. Allali, N. Dege, N. Benchat, S.A. Brandán, Synthesis, crystal structure, spectroscopic studies, NBO, AIM and SQMFF calculations of new pyridazinone derivative, J. Mol. Struct. 1223 (2020) 129213.

[22] E. Romano, N. Issaoui, M.E. Manzur, S.A. Brandán, Properties and Molecular docking of Antiviral to COVID-19 Chloroquine combining DFT calculations with SQMFF approach, Int. J. Curr. Adv. Res. 9 (8A) (2020) 22862–22876.

[23] O. Noureddine, S. Gatfaoui, S.A. Brandan, A. Sagaama, H. Marouani, N. Issaoui, Experimental and DFT studies on the molecular structure, spectroscopic properties, and molecular docking of 4-phenylpiperazine-1-ium dihydrogen phosphate, J. Mol. Struct. 1207 (2020) 127762.

[24] S. Gatfaoui, Issaoui N., T. Roisnel, H. Marouani, A proton transfer compound template phenylethylamine: synthesis, a collective experimental and theoretical investigations, J. Mol. Struct. 1191 (2019) 183–196.

[25] A. Sagaama, N. Issaoui, Design, molecular docking analysis of an anti-inflammatory drug, computational analysis and intermolecular interactions energy studies of 1-benzothiophene-2-carboxylic acid, Comput. Biol. Chem. 88 (2020) 107348.

[26] A.D. Becke, Density-functional exchange-energy approximation with correct asymptotic behavior, Phys. Rev. A38 (1988) 3098–3100.

[27] C. Lee, W. Yang, R.G. Parr, Development of the Colle-Salvetti correlation-energy formula into a functional of the electron density, Phys. Rev. B37 (1988) 785–789.

[28] Bruker, APEX3, SAINT, SADABS & SHELXTL, Bruker AXS, Inc., Madison, WI, 2016.

[29] G.M. Sheldrick, Crystallographic Shelves: Space-Group Hierarchy Explained, Acta Cryst. A71 (2015) 3–8.

[30] G.M. Sheldrick, Crystal structure refinement with SHELXL, Acta Cryst. C71 (2015) 3–8.

[31] K. Brandenburg, H. Putz, DIAMOND, Crystal Impact GbR, Bonn, Germany, 2012.

[32] M.J. Frisch, G.W. Trucks, H.B. Schlegel, G.E. Scuseria, M.A. Robb, J.R. Cheeseman, G. Scalmani, V. Barone, B. Mennucci, G.A. Petersson, H. Nakatsuji, M. Caricato, X. Li, H.P. Hratchian, A.F. Izmaylov, J. Bloino, G. Zheng, J.L. Sonnenberg, M. Hada, M. Ehara, K. Toyota, R. Fukuda, J. Hasegawa, M. Ishida, T. Nakajima, Y. Honda, O. Kitao, H. Nakai, T. Vreven, J.A. Montgomery Jr., J.E. Peralta, F. Ogliaro, M. Bearpark, J.J. Heyd, E. Brothers, K.N. Kudin, V.N. Staroverov, R. Kobayashi, J. Normand, K. Raghavachari, A. Rendell, J.C. Burant, S.S. Iyengar, J. Tomasi, M. Cossi, N. Rega, J.M. Millam, M. Klene, J.E. Knox, J.B. Cross, V. Bakken, C. Adamo, J. Jaramillo, R. Gomperts, R.E. Stratmann, O. Yazyev, A.J. Austin, R. Cammi, C. Pomelli, J.W. Ochterski, R.L. Martin, K. Morokuma, V.G. Zakrzewski, G.A. Voth, P. Salvador, J.J. Dannenberg, S. Dapprich, A.D. Daniels, Ö. Farkas, J.B. Foresman, J.V. Ortiz, J. Cioslowski, D.J. Fox, Gaussian 09, Revision A.02, Gaussian, Inc., Wallingford CT, 2009.

[33] S. Miertus, E. Scrocco, J. Tomasi, Electrostatic interaction of a solute with a continuum, Chem. Phys. 55 (1981) 117–129.

[34] J. Tomasi, J. Persico, Molecular Interactions in Solution: An Overview of Methods Based on Continous Distributions of the Solvent, Chem. Rev. 94 (1994) 2027–2094.

[35] A.V. Marenich, C.J. Cramer, D.G. Truhlar, Universal solvation model based on solute electron density and a continuum model of the solvent defined by the bulk dielectric constant and atomic surface tensions, J. Phys. Chem. B113 (2009) 6378–6396.

[36] E.D. Glendening, J.K. Badenhoop, A.D. Reed, J.E. Carpenter, F. Weinhold, NBO 3.1; Theoretical Chemistry Institute, University of Wisconsin, Madison, WI, 1996.

[37] R.F.W. Bader, Atoms in Molecules, A Quantum Theory, Oxford University Press, Oxford, 1990 ISBN: 0198558651.

[38] F. Biegler-Köning, J. Schönbohm, D. Bayles, AIM2000; A Program to Analyze and Visualize Atoms in Molecules, J. Comput. Chem. 22 (2001) 545.

[39] B.H. Besler, K.M. Merz Jr, P.A. Kollman, Atomic charges derived from semiempirical methods, J. Comp. Chem. 11 (1990) 431–439.

[40] A.B. Nielsen, A.J. Holder, Gauss View 5.0, User's Reference, GAUSSIAN Inc., Pittsburgh, PA, 2008.

[41] P. Pulay, G. Fogarasi, G. Pongor, J.E. Boggs, A. Vargha, Combination of theoretical ab initio and experimental information to obtain reliable harmonic force constants. Scaled quantum mechanical (QM) force fields for glyoxal, acrolein, butadiene, formaldehyde, and ethylene, J. Am. Chem. Soc. 105 (1983) 7073.

[42] a) G. Rauhut, P. Pulay, Transferable scaling factors for density functional derived vibrational force fields, J. Phys. Chem. 99 (1995) 3093–3099; b) G. Rauhut, P. Pulay, J. Phys. Chem. 99 (1995) 14572.

[43] T. Sundius, Scaling of ab-initio force fields by MOLVIB, Vib. Spectrosc. 29 (2002) 89–95.

[44] G. Keresztury, S. Holly, G. Besenyei, J. Varga, A.Y. Wang, J.R. Durig, Vibrational spectra of monothiocarbamates-II. IR and Raman spectra, vibrational assignment, conformational analysis and *ab initio* calculations of *S*-methyl-*N*,*N*-dimethylthiocarbamate, Spectrochim. Acta 49A (1993) 2007–2026.

[45] D. Michalska, R. Wysokinski, The prediction of Raman spectra of platinum(II) anticancer drugs by density functional theory, Chem. Phys. Lett. 403 (2005) 211–217.

[46] R. Ditchfield, Self-consistent perturbation theory of diamagnetism. I. A gage-invariant LCAO (linear combination of atomic orbitals) method for NMR chemical shifts, Mol Phys 27 (1974) 714–722.

[47] P. Ugliengo, MOLDRAW Program, Dipartimento Chimica IFM, Torino, Italy, University of Torino, 1998.

[48] D.F. Veber, S.R. Johnson, H-Y Cheng, R. Brian, K.W. Ward, K.D. Kopple, Molecular Properties that influence the oral bioavailability of drug candidates, J. Med. Chem. 45 (2002) 2615–2623.

[49] C.A. Lipinski, F. Lombardo, B.W. Dominy, P.J. Feeney, Experimental and computational approaches to estimate solubility and permeability in drug discovery and development setting, Adv. Drug Deliv. Rev. 46 (2001) 3–26.

[50] O. Trott, A.J. Olson, AutoDock Vina: improving the speed and accuracy of docking with a new scoring function, efficient optimization, and multithreading, J. Comput. Chem. 31 (2010) 455–461.

[51] S.A. Brandán, Normal internal coordinates, Force fields and vibrational study of Species Derived from Antiviral adamantadine, Int. J. Quantum Chem. 120 (2020) e26425.

[52] M.J. Márquez, S.A. Brandán, DFT study of Species Derived from the Narcotic Antagonist Naloxone, Biointerface Res. Appl. Chem. 10 (2020) 8096–8116.

[53] M.E. Manzur, S.A. Brandán, S(-) and R(+) Species Derived from Antihistaminic Promethazine Agent: Structural and Vibrational Studies, Heliyon 5 (2019) e02322.

[54] M.J. Márquez, M.A. Iramain, S.A. Brandán, *Ab-initio* and Vibrational studies on Free Base, Cationic and Hydrochloride Species Derived from Antihistaminic Cyclizine agent, Int. J. Sci. Res. 11 (2019) 53–87.

[55] S.A. Brandán, Why morphine is a molecule chemically powerful. Their comparison with cocaine, Indian J. Appl. Res. 7 (2017) 511–528.

[56] D. Romani, S.A. Brandán, Vibrational analyses of alkaloid cocaine as free base, cationic and hydrochloride species based on their internal coordinates and force fields, Paripex A, Indian J. Appl. Res. 6 (2017) 587–602.

[57] R.A. Rudyk, M.A. Checa, C.A.N. Catalán, S.A. Brandán, Structural, FT-IR, FT-Raman and ECD studies on the free base, cationic and hydrobromide species of scopolamine alkaloid, J Mol. Struct. 1180 (2019) 603–617.

[58] S.A. Brandán, Understanding the potency of heroin against to morphine and cocaine, Int. J. Sci. Res. 12 (2) (2018) 97–140.

[59] R.A. Rudyk, S.A. Brandán, Force field, internal coordinates and vibrational study of alkaloid tropane hydrochloride by using their infrared spectrum and DFT calculations, Indian J. Appl. Res. 6 (2017) 616–623.

[60] D. Romani, M.J. Márquez, M.B. Márquez, S.A. Brandán, Structural, topological and vibrational properties of an isothiazole derivatives series with antiviral activities, J. Mol. Struct. 1100 (2015) 279–289.

[61] D. Romani, O. Noureddine, N. Issaoui, S.A. Brandán, Properties, Reactivities and Molecular docking of Potential Antiviral to Treatment of COVID-19 Niclosamide in different media, Biointerface Res. Appl. 10 (2020) 7295–7328.

[62] M.B. Márquez, S.A. Brandán, A structural and vibrational investigation on the antiviral deoxyribonucleoside thymidine agent in gas and aqueous solution phases, Int. J. Quantum Chem. 114 (2014) 209–221.

[63] M.F. Ladetto, M.J. Márquez, D. Romani, S.A. Brandán, Structural and vibrational properties of the antiviral ribavirin drug in gas and aqueous environmental.

A complete assignment of their vibrational spectra, J. Adv. Chem. 16 (2019) 6325–6353.
[64] D. Romani, S.A. Brandán, Effect of the side chain on the properties from cidofovir to brincidofovir, an experimental antiviral drug against to Ebola virus disease, Arabian J. Chem. 12 (2019) 2959–2972.
[65] M.A. Iramain, S.A. Brandán, Structural and vibrational study on the acid, hexa-hydrated and anhydrous trisodic salts of antiviral drug Foscarnet, Drug Designing & Intellectual Properties International Journal 1 (2018) 1–17.
[66] L.V. de Freitas, C.C. da Silva, J. Ellena, L.A.S. Costa, N.A. Rey, Structural and vibrational study of 8-hydroxyquinoline-2-carboxaldehyde isonicotinoylhydrazone–A potential metal–protein attenuating compound (MPAC) for the treatment of Alzheimer's disease, Spectrochim. Acta A. 116 (2013) 41–48.
[67] N. Issaoui, N. Rekik, B. Oujia, M.J. Wójcik, Anharmonic effects on theoretical IR line shapes of medium strong H (D) bonds, Int. J. Quantum Chem. 109 (2009) 483–499.
[68] N. Issaoui, N. Rekik, B. Oujia, M.J. Wójcik, Theoretical infrared line shapes of H-bonds within the strong anharmonic coupling theory and Fermi resonances effects, Int. J. Quantum Chem. 110 (2010) 2583–2602.
[69] T. Benković, A. Kenđel, J. Parlov-Vuković, D. Kontrec, V. Chiş, S. Miljanić, N. Galić, Aromatic hydrazones derived from nicotinic acid hydrazide as fluorimetric pH sensing molecules: Structural analysis by computational and spectroscopic methods in solid phase and in solution, Spectrochim. Acta. Part A. 190 (2018) 259–267.
[70] D. Michalska, D.C. Bieńko, A.J. Abkowicz-Bieńko, Z. Latajka, Density functional, Hartree− Fock, and MP2 studies on the vibrational spectrum of phenol, J. Phys. Chem. 100 (1996) 17786–17790.
[71] C. Arunagiri, A.G. Anitha, A. Subashini, S. Selvakumar, Synthesis, X-ray crystal structure, vibrational spectroscopy, DFT calculations, electronic properties and Hirshfeld analysis of (E)-4-Bromo-N'-(2, 4-dihydroxy-benzylidene) benzohydrazide, J. Mol. Struct. 1163 (2018) 368–378.
[72] S.R. Sheeja, N.A. Mangalam, M.P. Kurup, Y.S. Mary, K. Raju, H.T. Varghese, C.Y. Panicker, Vibrational spectroscopic studies and computational study of quinoline-2-carbaldehyde benzoyl hydrazone, J. Mol. Struct. 973 (2010) 36–46.
[73] M. Turner, J. McKinnon, S. Wolff, D. Grimwood, P. Spackman, D. Jayatilaka, M. Spackman, CrystalExplorer17, University of Western Australia, Crawley, WA, Australia, 2017.
[74] F.L. Hirshfeld, Bonded-atom fragments for describing molecular charge densities, Theor. Chim. Acta. 44 (1977) 129–138.
[75] M.A. Spackman, D. Jayatilaka, Hirshfeld surface analysis, CrystEngComm 11 (2009) 19–32.
[76] A.C. Anderson, The process of structure-based drug design, Chem. Biol. 10 (2003) 787–797.
[77] D. Gilbert, Bioinformatics software resources, Brief. Bioinform. 5 (2004) 300–304.
[78] https://www.rcsb.org/.
[79] R.R. Narkhede, R.S. Cheke, J.P. Ambhore, S.D. Shinde, The Molecular Docking Study of Potential Drug Candidates Showing Anti-COVID-19 Activity by Exploring of Therapeutic Targets of SARS-CoV-2, screening, 5-8.
[80] http://www.3dsbiovia.com/.
[81] C.D. Owen, Lukacik, P., Strain-, C.M. Damerell, Douangamath, A., A.J. Powell, Fearon, D., Brandao-, J. Neto, Crawshaw, A.D., Aragao, W. D., M., Flaig, R., Hall, D.K. McAauley, Stuart, D.I., von Delft, W. F., M.A., COVID-19 main protease with unliganded active site, to be published.
[82] K. Michalska, Kim, Y., Jedrzejczak, R., Maltseva, N., Endres, M., Mececar, A., Joachimiak, A., Center for Structural Genomics of Infectious Diseases (CSGID), Crystal Structure of ADP ribose phosphatase of NSP3 from SARS-CoV-2 in complex with MES, to be published.